ARTICLE

Deacetylation of Miro1 by HDAC6 blocks mitochondrial transport and mediates axon growth inhibition

Ashley L. Kalinski[1,2]*, Amar N. Kar[3]*, John Craver[3], Andrew P. Tosolini[4], James N. Sleigh[4,5], Seung Joon Lee[3], Alicia Hawthorne[6], Paul Brito-Vargas[3], Sharmina Miller-Randolph[3], Ryan Passino[2], Liang Shi[3], Victor S.C. Wong[7], Cristina Picci[7], Deanna S. Smith[3], Dianna E. Willis[7], Leif A. Havton[8], Giampietro Schiavo[4,5,9], Roman J. Giger[2], Brett Langley[7], and Jeffery L. Twiss[3]

Inhibition of histone deacetylase 6 (HDAC6) was shown to support axon growth on the nonpermissive substrates myelin-associated glycoprotein (MAG) and chondroitin sulfate proteoglycans (CSPGs). Though HDAC6 deacetylates α-tubulin, we find that another HDAC6 substrate contributes to this axon growth failure. HDAC6 is known to impact transport of mitochondria, and we show that mitochondria accumulate in distal axons after HDAC6 inhibition. Miro and Milton proteins link mitochondria to motor proteins for axon transport. Exposing neurons to MAG and CSPGs decreases acetylation of Miro1 on Lysine 105 (K105) and decreases axonal mitochondrial transport. HDAC6 inhibition increases acetylated Miro1 in axons, and acetyl-mimetic Miro1 K105Q prevents CSPG-dependent decreases in mitochondrial transport and axon growth. MAG- and CSPG-dependent deacetylation of Miro1 requires RhoA/ROCK activation and downstream intracellular Ca^{2+} increase, and Miro1 K105Q prevents the decrease in axonal mitochondria seen with activated RhoA and elevated Ca^{2+}. These data point to HDAC6-dependent deacetylation of Miro1 as a mediator of axon growth inhibition through decreased mitochondrial transport.

Introduction

Inhibitory proteins in the extracellular matrix and myelin of the central nervous system (CNS) have been implicated in failed axon regeneration after spinal cord injury and brain trauma. These CNS growth inhibitors include myelin-associated glycoprotein (MAG) and chondroitin sulfate proteoglycans (CSPGs), which share several signaling pathways including activation of the small G-protein RhoA, which in turn triggers actin depolymerization and growth cone collapse (Schweigreiter et al., 2004). Blocking activation of RhoA, inhibiting RhoA's downstream Rho-associated protein kinase (ROCK), and increasing intracellular cAMP levels have all been shown to overcome the growth inhibitory effects of these nonpermissive substrates (Cai et al., 2001; Fournier et al., 2003; Duffy et al., 2009; Joshi et al., 2015). These MAG and CSPG signaling pathways have been intensely investigated as potential targets to support neural repair in the CNS, but it is not entirely clear what regulatory proteins

function downstream of MAG and CSPG beyond the effects of RhoA/ROCK on the axonal cytoskeleton.

Histone deacetylase 6 (HDAC6) was identified as a tubulin deacetylase, and HDAC6 knockout mice show hyperacetylation of α-tubulin (Zhang et al., 2008). Although better known for their nuclear functions, HDACs can function in the cytoplasm and target numerous proteins. Class II HDACs shuttle between the nucleus and cytoplasm (IIa includes HDACs 4, 5, 7, and 9, and IIb includes HDACs 6 and 10; Hubbert et al., 2002; Lahm et al., 2007). HDAC6 localizes into neuronal processes, and we previously showed that inhibition of HDAC6 supports axon growth on MAG and CSPGs (Rivieccio et al., 2009). α-Tubulin is a well-known substrate for HDAC6 (Hammond et al., 2008), and acetylation of α-tubulin is associated with more stable microtubules. Stabilizing microtubules in the injured spinal cord has been shown to reduce axon degeneration, prevent end bulb

[1]Department of Biology, Drexel University, Philadelphia, PA; [2]Department of Cell and Developmental Biology, University of Michigan, Ann Arbor, MI; [3]Department of Biological Sciences, University of South Carolina, Columbia, SC; [4]Department of Neuromuscular Diseases, UCL Queen Square Institute of Neurology, University College London, London, UK; [5]UK Dementia Research Institute, University College London, London, UK; [6]Department of Cell Biology, Emory University, Atlanta, GA; [7]Burke Neurological Institute, White Plains, NY; [8]Departments of Neurology and Neurobiology, University of California, Los Angeles, Los Angeles, CA; [9]Discoveries Centre for Regenerative and Precision Medicine, University College London Campus, London, UK.

*A.L. Kalinski and A.N. Kar contributed equally to this paper; Correspondence to Jeffery L. Twiss: twiss@mailbox.sc.edu; A. Hawthorne's present address is University of South Florida, Orlando, FL; L. Shi's present address is Augusta University, Augusta, GA; C. Picci's present address is University of Waikato, Hamilton, New Zealand; B. Langley's present address is University of Waikato, Hamilton, New Zealand.

formation typically seen in nonpermissive environments, and support axon regeneration (Hellal et al., 2011; Ruschel et al., 2015). We recently showed that MAG and CSPG decrease stability of α-tubulin acetyltransferase (αTAT), suggesting that the balance in activity of tubulin acetylating and deacetylating enzymes contributes to axon growth on nonpermissive substrates (Wong et al., 2018). However, HDAC6 obviously has other substrates in axons that could contribute to axon growth failure. Here, we show that both CSPGs and MAG attenuate axonal transport of mitochondria and decrease mitochondrial membrane potential, and these effects are prevented by inhibition of HDAC6. By use of pharmacological inhibitors, activators, and cytoplasmic Ca^{2+} level modulators, our data indicate that MAG- and CSPG-dependent activation of RhoA with subsequent increase in cytoplasmic Ca^{2+}, converge on HDAC6 to cause deacetylation of Miro1 on lysine 105 (K105), thereby blocking microtubule-dependent transport of axonal mitochondria. These data show that signaling mechanisms downstream of MAG and CSPGs attenuate mitochondrial transport and axon growth through a pathway that converges on HDAC6 for deacetylation of Miro1. Increasing acetyl-Miro1 levels supports axon growth by sustaining mitochondrial transport and mitochondrial membrane potential in the face of CNS axon growth inhibitors.

Results

HDAC6 inhibition increases growth cone size of sensory axons
Given our previous work showing that HDAC6 inhibition allows axons to grow on MAG and CSPG substrates (Rivieccio et al., 2009; Butler et al., 2010), we asked how inhibition of HDAC6 alters axon growth in cultures of adult dorsal root ganglion (DRG) neurons. After overnight culture on laminin, dissociated adult DRGs were treated for 1 h with 10 μM tubastatin (TubA), a concentration that was previously reported to selectively inhibit HDAC6 (Rivieccio et al., 2009; Butler et al., 2010). TubA treatment did not significantly affect neurite length compared with vehicle-treated DRG neurons (Fig. 1 A). However, the TubA-exposed DRG neurons showed significantly larger growth cones than the vehicle controls (Fig. 1, B and C), and this growth cone enlargement was apparent within 10 min of TubA exposure (Fig. 1 D). Both endogenous and transfected HDAC6 consistently concentrate in distal axons, including beyond the neurofilament (NF) signals into the growth cones of cultured DRG neurons (Figs. 1 E and S1 A).

Our previous work in rat embryonic cortical neurons had shown that 10 μM TubA increases levels of acetyl (Ac) α-tubulin but has no effect on histone acetylation, suggesting it is selective for HDAC6 over other HDACs (Rivieccio et al., 2009). We tested for this specificity in the adult DRG neurons from above by immunoblotting. Scriptaid, a pan-HDAC inhibitor, caused a clear increase in Ac-histone H4 levels, but 100 μM TubA caused only modest increase in Ac-histone H4, and no change in Ac-histone H4 levels were seen with 1 and 10 μM TubA or 6.3 μM Nullscript, a nonfunctional analogue of Scriptaid (Fig. S1, B and C). However, 1, 10, and 100 μM TubA caused a clear increase in Ac-α-tubulin levels (Fig. S1, B and C). By immunolabeling, a
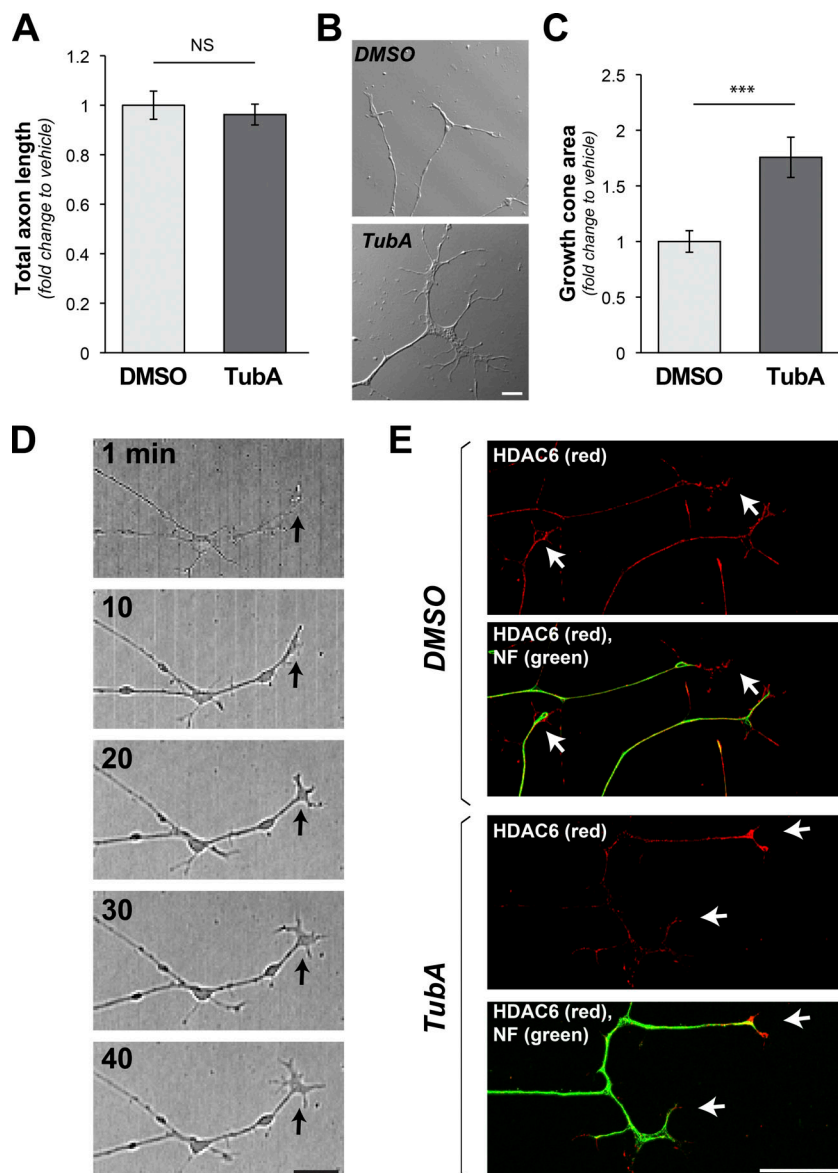
significant increase in anti–Ac-α-tubulin immunoreactivity in growth cones was seen with 10 μM TubA compared with control cultures, with no change in tyrosinated α-tubulin (Fig. S2, A–C). Along with the increased Ac-α-tubulin, growth cone signals for F-actin were consistently decreased in the TubA-treated cultures (Fig. S2, A and D). These data indicate rapid changes in cytoskeletal dynamics of the distal axons upon HDAC6 inhibition.

Mitochondria accumulate in growth cones after HDAC6 inhibition
HDAC6 inhibition was previously shown to increase transport of mitochondria in axons of embryonic rodent hippocampal and chick sensory neurons (Chen et al., 2010; Kim et al., 2012; Rui and Zheng, 2016; Sainath et al., 2017), and axonal mitochondrial transport has been linked to axon growth (Steketee et al., 2012; Cartoni et al., 2016; Lewis et al., 2016; Zhou et al., 2016). By live-cell imaging with MitoTracker to visualize mitochondria, DRG neurons appeared to show increased anterograde versus retrograde mitochondrial movement along axons (Fig. S3, A and B). There were no significant differences in the speed, track durations, or directionality for axonal mitochondrial movements (Fig. S3, C–E), but there was a significant increase in mitochondrial profiles in the growth cones of the HDAC6-inhibited cultures (Fig. 2 A), and the HDAC6-inhibited cultures consistently showed more anterogradely than retrogradely moving mitochondria in axons (Fig. S3 E). To determine if TubA might also affect axonal mitochondria in vivo, we directly injected TubA into the sciatic nerve of adult rats at mid-thigh. Analysis of nerves immediately adjacent to the injection sites by EM 2 h after injection showed that mitochondrial numbers in the vehicle-treated nerves were not significantly different than nerves that were not manipulated, indicating that the trauma from injection did not affect number of mitochondria in unmyelinated axons (i.e., naive nerves; Fig. 2, B and C). However, the nerve exposed to TubA showed significantly increased mitochondrial numbers in the unmyelinated axons, where we surmise the TubA and DMSO vehicle would have greatest penetration in these intact adult nerves (Fig. 2, B and C). As this could reflect stalling of mitochondria or increased numbers of anterogradely and/or retrogradely moving mitochondria, we performed in vivo imaging to visualize mitochondrial dynamics. Similar to the kinetic analyses in cultured primary neurons, the ratio of anterogradely to retrogradely moving axonal mitochondria increased with TubA (Fig. 2, D and E), but neither this nor the speed of movement showed significant differences compared with vehicle control (Fig. S3, F and G). However, there was significantly increased pausing for retrogradely versus anterogradely moving mitochondria after exposure to TubA (Fig. 2 F). Together, these experiments indicate that HDAC6 activity impacts axonal mitochondrial transport in vitro and in vivo.

HDAC6 inhibition or depletion protects axons from mitochondrial damage
Studies in several neuronal systems have shown the importance of mitochondrial respiration and transport in axon growth

Kalinski et al.
Deacetylation of Miro1 by HDAC6

Journal of Cell Biology
https://doi.org/10.1083/jcb.201702187

1872

Figure 1. **Growth cones expand on inhibition of HDAC6. (A)** Quantification of neurite length for dissociated DRGs cultured on laminin with addition of HDAC6 inhibitor TubA (10 µm) versus vehicle control (DMSO) over 1 h is shown as average fold-change relative to vehicle ± SEM ($n \geq 95$ neurons across three independent experiments; NS by one-way ANOVA with Bonferroni post hoc). **(B and C)** Representative DIC images of distal axons from DRG neurons cultured as in A are shown (B). 1-h TubA treatment appears to increase growth cone size. Analyses of growth cone area across multiple experiments show a significant increase in area after TubA treatment (C). Values are average fold-change ± SEM ($n \geq 26$ neurons over at least three culture preparations; ***, $P \leq 0.005$ by one-way ANOVA with Bonferroni post hoc; scale bar = 5 µm; 40×/1.3 NA objective used). **(D)** Representative time-lapse image sequence in DIC for a single axon from larger tiled images after addition of TubA as in A. Arrows indicate growth cone position (scale bar = 10 µm). **(E)** Representative epifluorescent images for HDAC6 (red, Cy5) and NF (green, Cy3) immunoreactivity. Prominent HDAC6 signals are seen in distal axons and growth cones (arrows) regardless of TubA exposure. Axonal localization of transfected HDAC6 protein is shown in Fig. S1 A (scale bar = 10 µm; 40×/1.3 NA objective used).

(Steketee et al., 2012; Cartoni et al., 2016; Lewis et al., 2016; Zhou et al., 2016). The mitochondrial transport dynamics above showed a relative increase in anterograde versus retrograde movement, but this was overall modest. Nonetheless, the accumulation of mitochondria in growth cones could be reflective of this shift, so we asked if the growth cone accumulation of mitochondria seen after HDAC6 inhibition has any biological significance. For this, we turned to chromophore-assisted light inactivation (CALI) to ablate mitochondria from distal axons of DRG cultures expressing mitochondrial-targeted Killer Red (Mito-KR) protein. CALI of KR protein generates reactive oxygen species (ROS) to ~1,000-fold higher than the fluorescent emission eGFP generates (Sano et al., 2014). Increased ROS production upon CALI of Mito-KR protein leads to mitochondrial damage and ablation of mitochondrial function, including the axonal mitochondria targeted in our experiments (Shibuya and Tsujimoto, 2012; Spillane et al., 2013). Since TubA treatment expanded growth size and altered mitochondrial transport, we

attempted to choose axons for these CALI experiments that were matched for growth cone size and mito-KR signal intensity; analyses of average growth cone areas and Mito-KR fluorescent intensities showed no significant differences between control and TubA-treated axons tested in the pre-CALI time points (Fig. S4, A and B). Approximately 85% of axons subjected to CALI in the vehicle-treated cultures showed rapid growth cone retraction (Fig. 3, A–D). In contrast, the majority of the TubA-treated cultures showed no growth cone retraction after CALI (Fig. 3, A–D), and the distal axons showed significant recovery of mitochondrial fluorescence in the bleached region of interest (ROI) after CALI compared with vehicle-treated cultures (Fig. 3 E).

Although the 10-µM TubA dose clearly increases levels of Ac-α-tubulin by immunoblotting and immunofluorescence (Figs. S1 and S2), we sought to exclude the possibility that off-target effects of TubA might cause these effects on mitochondria. Thus, we applied this CALI approach to DRGs that were also co-transfected with HDAC6 or control siRNAs (siHDAC6 and
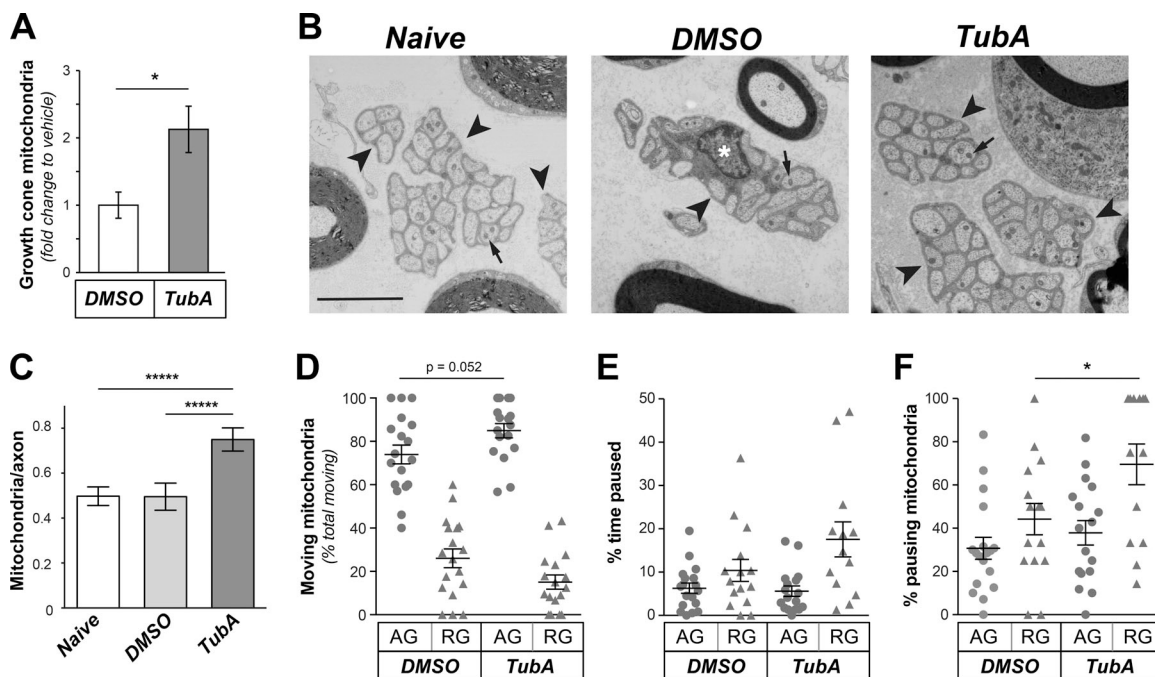
Figure 2. **Inhibition of HDAC6 alters axonal mitochondrial transport both in vitro and in vivo. (A)** Number of mitochondria in growth cones after exposing DRG cultures to 10 µM TubA versus vehicle (control) for 1 h is shown as average fold-change in number of mitochondria per growth cone ± SEM ($n = 13$ axons across three culture preparations; *, $P \leq 0.05$ by one-way ANOVA with Bonferroni post hoc analysis). See Fig. S3 (A–E) for kinetics of mitochondria movement in axons. **(B)** Representative EMs of Remak bundles (arrowheads) in naive Sciatic nerve and nerves after 2 h vehicle (DMSO) or TubA injection are shown. Arrows indicate mitochondria in the unmyelinated axons. Note that a Schwann cell nucleus (asterisk) is seen in the Remak bundle for DMSO image but not the other two micrographs (scale bar = 3 µm). **(C)** Quantification of number of mitochondria per unmyelinated axon from EM images as in B is shown as average ± SEM ($n \geq 5$; *****, $P \leq 0.0001$ by one-way ANOVA with Bonferroni post hoc analysis). **(D–F)** Quantification for indicated parameters for mitochondrial transport in sciatic nerve in vivo using tetramethylrhodamine, ethyl ester, perchlorate to visualize mitochondria is shown. The percentage pausing mitochondria is significantly different for retrogradely tracked mitochondria in DMSO versus TubA injected nerves ($n \geq 13$ axons tracked over four animals; *, $P \leq 0.05$ and as indicated by ANOVA with Holm-Sidak's multiple comparisons test).

siControl, respectively). siHDAC6 significantly depleted HDAC6 from the DRG neurons compared with the siControl (Fig. S4, C and D). siHDAC6-transfected cultures showed significantly less growth cone retraction after mitochondrial ablation with CALI, similar to the TubA-treated cultures (Fig. S4, E–G). The siHDAC6-transfected cultures also showed significantly greater Mito-KR fluorescent recovery in CALI ROI during the post-CALI period compared with the siControl-transfected cultures (Fig. S4 H). Since activation of the Mito-KR with CALI permanently ablates mitochondria, the fluorescent recovery of Mito-KR in the ROI likely represents transport of mitochondria from more proximal segments of the axon in the HDAC6-inhibited and HDAC6-depleted neurons. Although we cannot completely exclude increased uptake of Mito-KR in these neurons, data below using different mitochondria labeling methods are consistent with a net shift to increased anterograde movement of axonal mitochondrial when HDAC6 is inhibited.

MAG and CSPGs attenuate mitochondrial transport in axons through activation of RhoA

Inhibition of HDAC6 was shown to prevent axon retraction seen with exposure to MAG and CSPGs (Rivieccio et al., 2009), so we next asked if the recovery of mitochondria after CALI might be affected by recombinant human MAG as an Fc fusion or Fc control proteins (MAG-Fc and Fc, respectively). After 4-h exposure to MAG-Fc by bath application, DRG cultures showed significantly decreased recovery of Mito-KR fluorescence in the CALI ROI compared with Fc-exposed cultures, and this was reversed by treatment with TubA (Fig. 4 A). Since a difference in mitochondrial ROS release upon Mito-KR activation could impact transport of mitochondria and hence CALI recovery in the HDAC6-inhibited neurons, we expressed Mito-GFP and used traditional FRAP assays to compare recovery in MAG-Fc–treated versus Fc-treated cultures. Recovery of Mito-GFP fluorescent signals in the FRAP ROI was also significantly decreased in the distal axons of cultures treated with MAG-Fc compared with the control Fc, and this was prevented by TubA pretreatment (Figs. 4 B and S5 A). Bath application of the CSPG aggrecan similarly attenuated recovery of Mito-GFP fluorescence from FRAP of distal axons, and this was prevented by treatment with TubA (Fig. 4 C).

To determine if the effect of growth inhibitors on mitochondrial recovery was limited to distal axons, we performed FRAP on more proximal segments of the axon shaft in DRG neurons expressing Mito-GFP. For analyses of recovery, the bleached ROIs were divided into four subregions along the axon length so that we could distinguish anterograde from retrograde transport-driven Mito-GFP recovery (Fig. S5 B). Control cultures showed more rapid recovery in the distal bleached axon
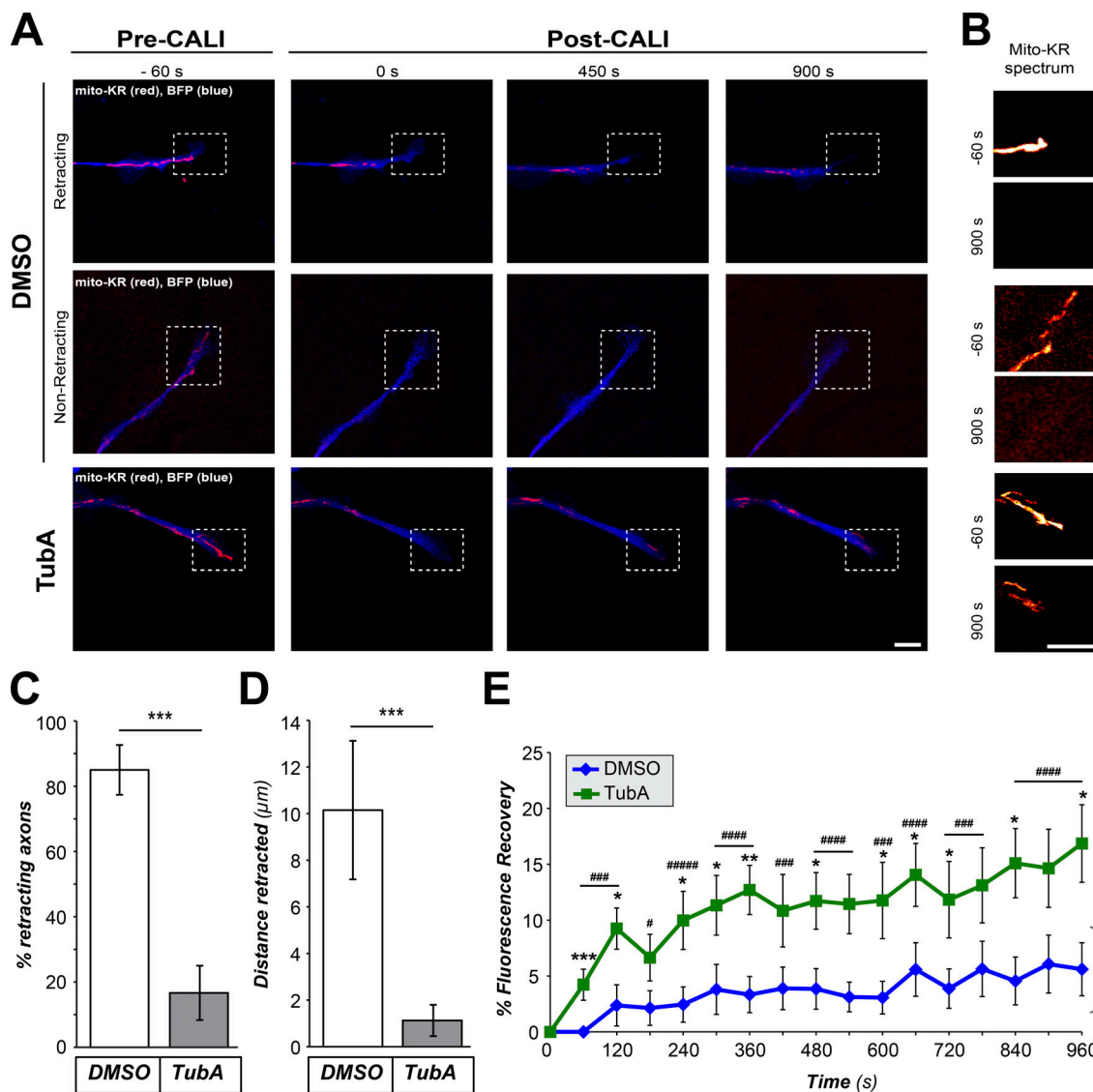
Figure 3. HDAC6-inhibited growth cones are protected from collapse after mitochondrial ablation. (A and B) Representative images from CALI time-lapse sequence are shown for DRGs cultured on laminin and treated with vehicle control (DMSO) versus 10 µM TubA for 1 h (A). BFP is shown in blue as an axonal marker and Mito-KR signal is shown in red. Boxed regions represent ROI for distal axon and growth cone that was subjected to photoactivation of Mito-KR to ablate mitochondria. **(B)** Magnified view of ROI with Mito-KR signal as indicated spectral intensity for −60-s and +900-s panels from time lapse. Fig. S4 (A and B) shows that axons analyzed across the DMSO- and TubA-treated cultures had no significant differences in growth cone area or Mito-KR signal intensity before CALI sequence. Images were equivalently adjusted for brightness and contrast before cropping using ImageJ (scale bars = 10 µm for main panels, 2 µm for insets; 63×/1.4 NA objective used). **(C and D)** Quantifications of percentage of axons retracting (C) and retraction distance (D) from image sequences as in A are shown as average ± SEM ($n \geq 13$ across three culture preparations; ***, $P \leq 0.005$ by one-way ANOVA with Bonferroni post hoc analysis). **(E)** Recovery of Mito-KR red fluorescence in photoactivated ROI from image sequences as in A is shown as average of normalized percentage recovery ± SEM ($n \geq 13$ axons from three independent experiments; *, $P \leq 0.05$; **, $P \leq 0.01$; ***, $P \leq 0.005$ vs. $t = 0$; ###, $P \leq 0.005$; ####, $P \leq 0.001$; #####, $P \leq 0.0005$ for TubA vs. control; and NS vs. $t = 0$ s by one-way ANOVA with Bonferroni post hoc analysis).

segment, and this was appreciably decreased by bath application of MAG-Fc (Fig. S5, Ci vs. Cii). In contrast, the TubA-treated cultures showed more rapid recovery in proximal segments (Fig. S5, Ciii), and MAG-Fc's attenuation of axonal Mito-GFP recovery was prevented by HDAC6 inhibition (Fig. S5, Civ vs. Cii). Since this effect of MAG-Fc on recovery could derive from either axons or cell body, we cultured dissociated DRGs in microfluidic devices where we could limit exposure to MAG-Fc and TubA to the axons. Consistent with MAG-Fc decreasing Mito-GFP fluorescent recovery in the proximally oriented axonal ROIs

in the above experiment, application of MAG-Fc to the axonal compartment decreased numbers of mitochondria in the distal axons, and this was prevented by TubA treatment (Fig. S5 D). TubA treatment also prevented the axon retraction and end bulb formation in distal axons that was seen after MAG-Fc exposure (Fig. S5 E). Localized exposure of axons to CSPG similarly decreased mitochondrial transport in axons (see Figs. S7 D and 7 G below). Taken together, these data suggest that the MAG- and CSPG-dependent effects on mitochondrial transport initiate from HDAC6 activity within the axon, as we previously showed
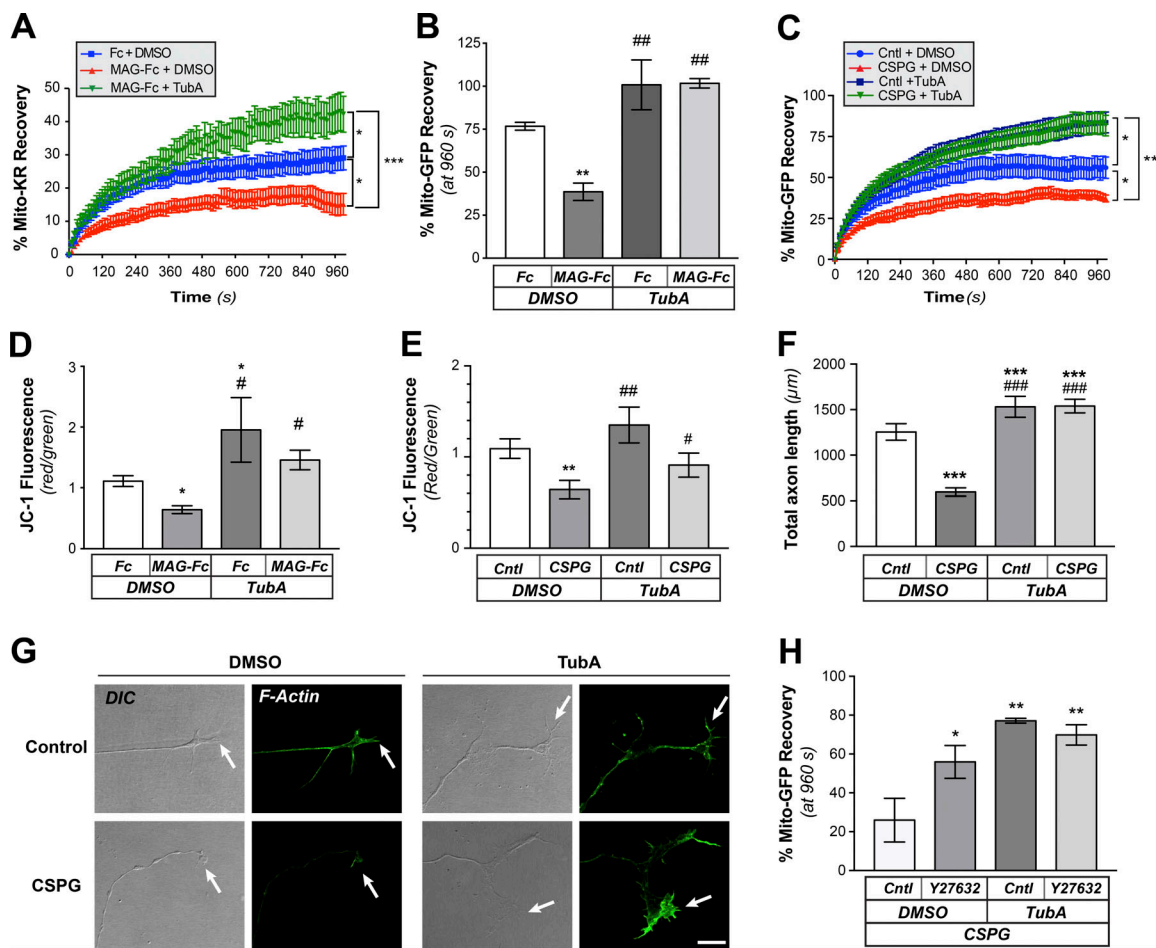
Figure 4. **MAG and CSPGs decrease mitochondrial transport through an HDAC6-dependent pathway. (A)** Recovery of Mito-KR signals after CALI to ablate mitochondria in distal axons of DRGs cultured on laminin and exposed to vehicle control (DMSO) or to bath-applied Fc + DMSO, MAG-Fc + DMSO or MAG-Fc + 10 µm TubA. Values represent average of normalized percentage recovery ± SEM ($n \geq 16$ axons over five culture preparations; *, P ≤ 0.05; ***, P ≤ 0.005 for indicated treatments by two-way ANOVA with Tukey post hoc). Fc + DMSO was not significantly different than vehicle control (not depicted). **(B)** End-point FRAP analysis for Mito-GFP in distal axons of DRGs cultured on laminin and treated bath-applied Fc vs. MAG-Fc as in A is shown as average of normalized percentage recovery ± SEM at 960 s after bleach ($n \geq 12$ axons over four culture preparations; **, P ≤ 0.05 vs. Fc-control; ##, P ≤ 0.01 vs. MAG + vehicle by two-way ANOVA with Tukey post hoc). Fig. S5 A shows full analysis of the FRAP sequences. **(C)** FRAP analysis for Mito-GFP recovery in distal axons of DRGs cultured on laminin and treated with ±10 µg/ml bath-applied aggrecan (Cntl or CSPG) and 10 µM TubA or vehicle control (DMSO) is shown as average of normalized percentage recovery ± SEM at 960 s after bleach ($n \geq 16$ axons over four culture preparations; *, P ≤ 0.05 for control + DMSO vs. control + TubA and control + DMSO vs. CSPG + DMSO; ***, P ≤ 0.005 for CSPG + DMSO vs. CSPG + TubA and CSPG + DMSO vs. control + TubA by two-way ANOVA with Tukey post hoc). **(D and E)** Mitochondrial membrane potential was assessed in axon shafts of DRGs cultured on laminin and then treated with bath-applied MAG-Fc (D) or aggrecan (CSPG; E) as in A and C. Values indicate average ratio of normalized red/green fluorescence signals ± SEM within the ROIs after indicated treatments ($n \geq 25$ axons over four culture preparations; *, P ≤ 0.05; **, P ≤ 0.01 vs. DMSO; #, P ≤ 0.05; ##, P ≤ 0.01 vs. MAG + DMSO or CSPG + DMSO by two-way ANOVA with Tukey post hoc). **(F)** Quantitation of axon growth for DRGs cultured on laminin (Cntl) or substrate-bound aggrecan (CSPG) and treated with DMSO or 10 µM TubA. Axon growth was assessed at 24 h and is shown as average total length/neuron ± SEM ($n \geq 95$ each over three DRG cultures; ***, P ≤ 0.005 vs. control; ###, P ≤ 0.005 vs. CSPG + vehicle by two-way ANOVA with Tukey post hoc). **(G)** Representative DIC and F-actin (green, Alexa Fluor 555) images of distal axons from DRGs cultured on laminin and treated with 10 µM TubA or vehicle control (DMSO) are shown before and after bath-applied 10 µg/ml aggrecan (CSPG). Arrows mark axon termini. Images were cropped from larger panels to highlight growth cones using ImageJ (scale bar = 10 µm; 63×/1.4 NA objective used). **(H)** End-point FRAP analyses for Mito-GFP in distal axons of DRGs cultured on laminin and treated with bath-applied 10 µg/ml aggrecan are shown as average of normalized percentage recovery ± SEM at 960 s after bleach. To test for effects of ROCK inhibition, neurons were pretreated with vehicle (Cntl) or 10 µM Y27632. To test for potential synergism with HDAC6 inhibition, control and Y27632-treated cultures were exposed to DMSO or 10 µM TubA ($n \geq 16$ axons over four culture preparations; *, P ≤ 0.05; **, P ≤ 0.005 for indicated treatments by two-way ANOVA with Tukey post hoc).

for HDAC6's role in MAG- and CSPG-dependent axon growth inhibition (Rivieccio et al., 2009).

Considering the above changes in mitochondrial transport, we asked if MAG and CSPG might affect mitochondrial function in axons. Functional mitochondria are needed to generate ATP, and the mitochondrion's membrane potential (ψ_M) is thought to reflect its capacity for generating ATP. Increased anterograde transport of mitochondria in axons correlated with higher ψ_M, as measured by the ratiometric 5,5′,6,6′-tetrachloro-1,1′,3,3′-tetraethylbenzimidazolcarbocyanine iodide (JC-1) dye (Miller and Sheetz, 2004), and reduced axonal ψ_M in *Drosophila melanogaster* larvae was recently correlated with overall decrease in

mitochondrial transport (Liao et al., 2017). Interestingly, there was a significant decrease in ψ_M in DRG cultures after bath application of MAG-Fc or CSPG (Fig. 4, D and E). These declines in ψ_M were prevented by inhibition of HDAC6 with TubA. This suggests that there is an HDAC6-dependent decrease in mitochondrial respiration upon exposure to CNS growth inhibitory proteins.

MAG and CSPGs are more often tested as surface-bound substrates than with the bath applications used here. Thus, we tested whether bath application of growth inhibitors would cause growth cone retraction in a manner similar to surface-bound inhibitors. As expected, the aggrecan used here attenuated axon growth when bound to coverslips, and this was prevented by TubA exposure (Fig. 4 F). Bath application of aggrecan at doses used in the experiments above caused rapid retraction of growth cones, and this was prevented by application of TubA (Fig. 4 G). Similar effects were observed for bath applied MAG-Fc (not depicted). RhoA activation is a well-known downstream mediator for the growth-inhibitory effects of both MAG and CSPGs (Fujita and Yamashita, 2014), so we tested whether the RhoA/ROCK pathway contributes to the impact of aggrecan on mitochondria distribution in growth cones. Pharmacological inhibition of ROCK with Y27632 prevented the aggrecan-dependent decrease in Mito-GFP recovery in distal axons after photobleaching (Fig. 4 H), indicating that the RhoA/ROCK pathway is involved in reducing mitochondrial transport into axons in response to aggrecan. Interestingly, no significant additive effects were seen when the ROCK inhibitor was combined with 10 µM TubA (Fig. 4 H). ROCK inhibition similarly blocked the decline in mitochondrial transport in response to MAG-Fc, and there was no additive or synergistic effect when combined with TubA treatment (see Fig. 5 B below). Taken together, these data raise the possibility that decreases in mitochondrial transport and ψ_M contribute to HDAC6-dependent attenuation of axon growth after exposure to CNS growth inhibitors through a RhoA/ROCK signaling pathway.

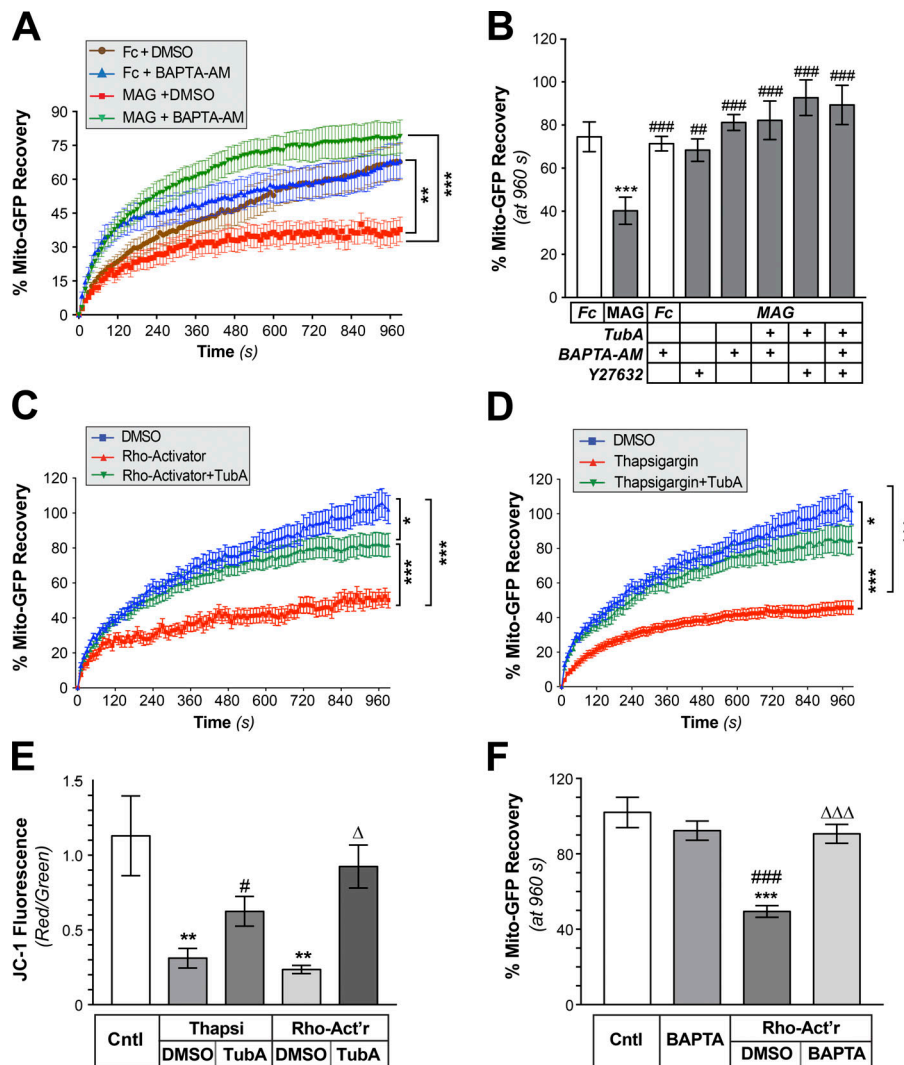## Ca²⁺ is downstream of RhoA for HDAC6-dependent attenuation of mitochondrial transport by CNS growth inhibitors

Both MAG and CSPGs are known to increase axoplasmic $[Ca^{2+}]$ (Snow et al., 1994; Henley et al., 2004), and increased cytoplasmic Ca^{2+} has been shown to decrease microtubule-based transport of mitochondria (Lin and Sheng, 2015). To test the potential contribution of Ca^{2+} in attenuating axonal mitochondrial transport after exposure to CNS growth inhibitors, we used BAPTA-AM to chelate intracellular Ca^{2+}. We initially titrated successively lower BAPTA-AM concentrations to reach a concentration with minimal effects on basal mitochondrial transport. At 3 µM BAPTA-AM, mitochondria showed increased recovery in the distal axons over the first 5 min after bleach, but FRAP recovery was no different than recovery in untreated cultures thereafter (Fig. 5 A). 3 µM BAPTA-AM prevented the MAG-Fc attenuation of axonal mitochondrial transport, comparing recoveries as end-point values (i.e., at 960 s after bleach; Fig. 5, A and B). No significant additive effects were seen when combining 3 µM BAPTA-AM with 10 µM TubA (Fig. 5 B). ROCK

inhibition similarly prevented the MAG-dependent decrease in mitochondrial transport, and there was no additive or synergistic effect when ROCK inhibition was combined with 3 µM BAPTA-AM (Fig. 5 B). Finally, combined treatment with 10 µM TubA, 3 µM BAPTA-AM, and ROCK inhibitor did not increase mitochondrial transport above the results seen with HDAC6 inhibition, Ca^{2+} chelation, or ROCK inhibition alone (Fig. 5 B). These observations raise the possibility of a signaling pathway involving RhoA/Rock activation and increased cytoplasmic $[Ca^{2+}]$ for HDAC6 activation and decreased mitochondrial transport in response to these CNS growth inhibitors.

Because it was also possible that we had simply reached a maximum rate of mitochondrial transport such that no additive or synergistic effects could be seen above with our FRAP-based assay, we directly activated RhoA or increased cytoplasmic $[Ca^{2+}]$ and tested for effects on axonal Mito-GFP transport and ψ_M. Application of the RhoA activator II compound (Flatau et al., 1997; Schmidt et al., 1997) decreased axonal mitochondrial transport, and this was prevented by treatment with TubA (Fig. 5 C). Releasing ER Ca^{2+} stores by treatment with thapsigargin similarly decreased mitochondrial transport in the DRG axons, and this was prevented by inhibition of HDAC6 (Fig. 5 D). Both the Rho activator and thapsigargin decreased ψ_M in the axons, which was also prevented by HDAC6 inhibition (Fig. 5 E). Finally, we directly tested whether Ca^{2+} could be downstream of RhoA activation in this signaling pathway. Chelation of intracellular Ca^{2+} with BAPTA-AM completely abrogated the decrease in axonal mitochondrial transport seen upon direct activation of RhoA (Fig. 5 F). Together, these data suggest that RhoA/ROCK activation followed by increase in axoplasmic Ca^{2+} decreases axonal mitochondria transport through an HDAC6-dependent pathway.

HDAC6 deacetylates Miro1 to modulate mitochondrial transport in axons

Considering that the studies above suggest that the decrease in mitochondrial transport seen after MAG and CSPG exposure is an HDAC6-dependent process, we next investigated what might lie downstream of HDAC6. Acetylated K40 in α-tubulin is a substrate for HDAC6 (Hubbert et al., 2002; Matsuyama et al., 2002; Zhang et al., 2003). Substitution of Gln for lysine has been reported to mimic acetylated Lys, and substitution of Ala for Lys generates a nonacetylatable protein (Li et al., 2002). We transfected DRG neurons with acetyl-mimetic K40Q and nonacetylatable K40A α-tubulin cDNA expression constructs to determine if HDAC6-dependent deacetylation of α-tubulin accounts for the above changes in mitochondrial transport. Despite that the K40A and K40Q α-tubulin-mCherry mutant proteins were clearly incorporated into microtubules in the axons of cultured DRGs at levels comparable to WT α-tubulin-mCherry protein (Fig. S6 A), HDAC6-dependent increases in axonal mitochondrial transport were still seen in DRGs expressing either nonacetylatable or acetyl-mimetic α-tubulin by FRAP assays (Fig. 6 A). This raises the possibility that HDAC6 substrates other than α-tubulin contribute to HDAC6's attenuation of mitochondrial transport. Ca^{2+}-dependent dissociation of the Miro/Milton protein complex, which links mitochondria to motor

Figure 5. **RhoA/ROCK pathway activates HDAC6 through a Ca²⁺-dependent mechanism. (A)** FRAP analyses for Mito-GFP in distal axons of DRGs cultured on laminin and treated with bath-applied Fc + DMSO, Fc + 3 µM BAPTA-AM, MAG-Fc + DMSO, or MAG-Fc + 3 µM BAPTA-AM are shown as average normalized percentage recovery ± SEM ($n \geq 9$ axons over three culture preparations; **, $P \leq 0.01$; ***, $P \leq 0.005$ for indicated treatments by two-way ANOVA with Tukey post hoc). BAPTA-AM is not statistically different from over 300 to 960 s. **(B)** End-point FRAP for Mito-GFP in distal axons of DRGs treated with bath-applied Fc vs. MAG-Fc ± 3 µM BAPTA-AM, 10 µM Y27632, 10 µM TubA, or indicated combinations of these inhibitors is shown as average of normalized percentage recovery ± SEM at 960 s after bleach ($n \geq 9$ axons over three culture preparations; ***, $P \leq 0.005$ vs. Fc; ##, $P \leq 0.01$; ###, $P \leq 0.005$ vs. Mag-treated by two-way ANOVA with Tukey post hoc). BAPTA-AM is not statistically different from vehicle. **(C and D)** FRAP for Mito-GFP in distal axons of DRGs treated with RhoA Activator (C) or Thapsigargin (D) is shown as average normalized percentage recovery ± SEM. Data for vehicle control (DMSO), 1 µg/ml of Rho-Activator (+ DMSO), Rho-Activator + 10 µM TubA, 1 µM Thapsigargin (+ DMSO), and Thapsigargin + 10 µM TubA are shown ($n \geq 9$ axons over three culture preparations; *, $P \leq 0.05$; ***, $P \leq 0.005$ for indicated treatments by two-way ANOVA with Tukey post hoc). **(E)** Quantification of mitochondrial membrane potential based on red/green fluorescence of JC-1 in axon shafts of DRGs cultured on laminin (Cntl) or aggrecan (CSPG) substrates is shown after treatment with 1 µM Thapsigargin (Thapsi), Thapsi + 10 µM TubA, 1 µg/ml Rho-Activator (Rho-Act'r), or Rho-Act'r + TubA. Values represent average ratio of normalized red/green fluorescent JC-1 signals ±

SEM ($n \geq 20$ axons over three culture preparations; **, $P \leq 0.01$ vs. control; #, $P \leq 0.05$ vs. Thapsi + DMSO; Δ, $P \leq 0.01$ vs. Rho-Act'r + DMSO by two-way ANOVA with Tukey post hoc). **(F)** End-point FRAP for Mito-GFP in distal axons of DRGs cultured on laminin and treated ± 3 µM BAPTA-AM, 1 µg/ml Rho-Act'r, Rho-Act'r + BAPTA-AM is shown as average of normalized percentage recovery ± SEM at 960 s after bleach ($n \geq 9$ axons over three culture preparations; ***, $P \leq 0.005$ vs. control; ###, $P \leq 0.005$ vs. BAPTA-AM; ΔΔΔ, $P \leq 0.005$ vs. Rho-Act'r + DMSO by two-way ANOVA with Tukey post hoc). BAPTA-AM is not statistically different from control.

proteins Lee and Lu, 2014, or activation of Syntaphilin protein, which docks mitochondria in axons and dendrites (Lin and Sheng, 2015), can decrease mitochondrial transport in axons. Protein acetylome profiles from nonneuronal cells have reported acetylation of Miro1/2 and Milton 1/2 but not of Syntaphilin (Choudhary et al., 2009; Lundby et al., 2012; Wagner et al., 2012). Of these, Miro1 showed the highest number of acetylation sites, with three separate sites reported. Consistent with this report, we see that mouse and rabbit anti–Ac-Lys antibody cocktail immunoprecipitates Miro1 from lysates of cultured DRGs, with the anti–Ac-Lys immunoprecipitated Miro1 band modestly increasing upon treatment with TubA (Fig. 6 B). Moreover, Miro1 and HDAC6 coimmunoprecipitate (Fig. 6 C), suggesting that these proteins do interact.
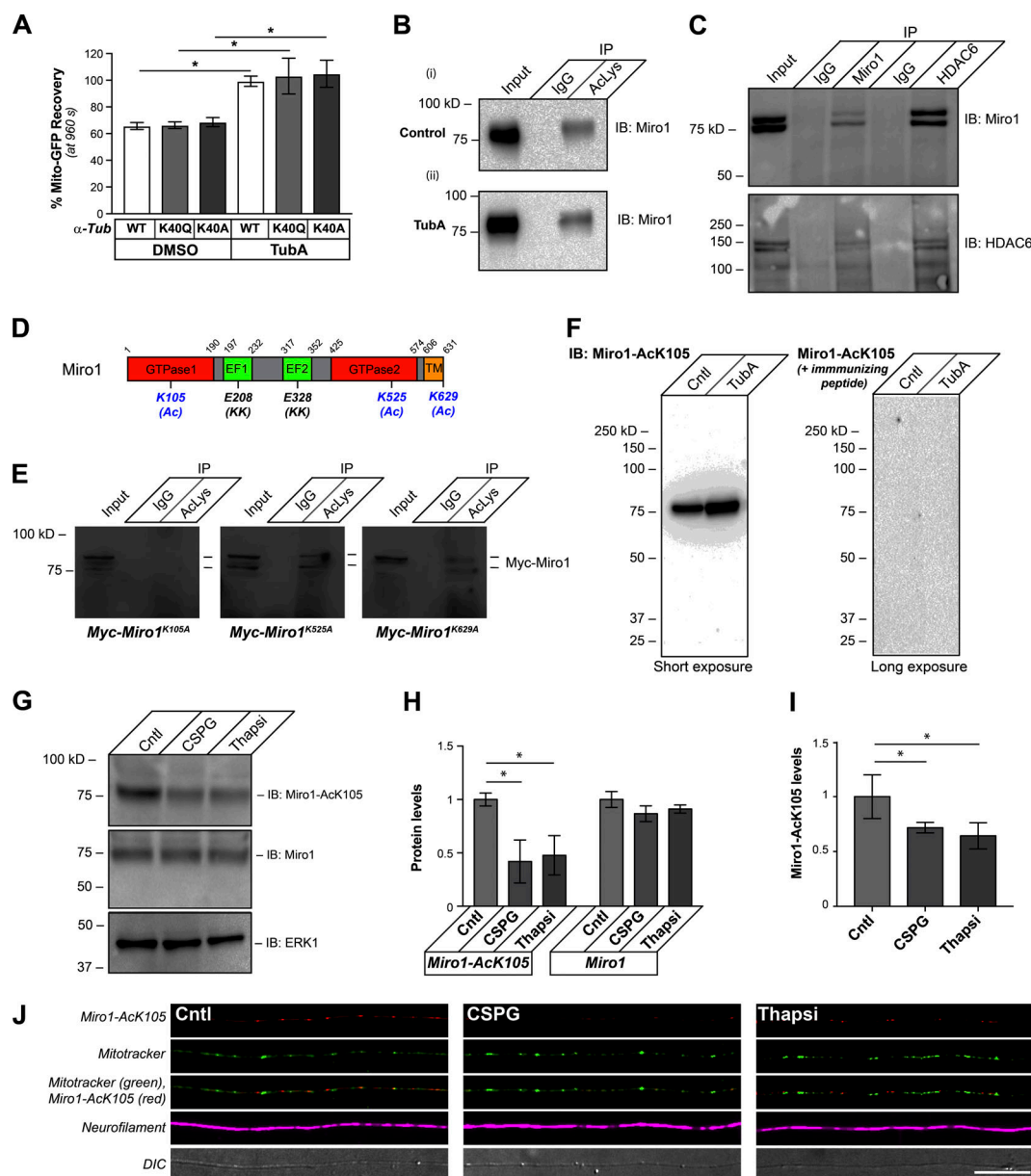
The three reported acetylation sites for Miro1 in human cell lines K92, K512, and K618 (Choudhary et al., 2009; Lundby et al., 2012) correspond to K105, K525, and K629 in rat Miro1 (Fig. 6 D).

We generated Lys-to-Ala mutants for K105, K525, and K629 to determine if these Miro1 residues are acetylated in neurons (Myc-Miro1^{K105A}, Myc-Miro1^{K525A}, and Myc-Miro1^{K629Q}; Fig. 6 D). Immunoprecipitation with anti–Ac-Lys antibodies showed that acetylation of myc-tagged Miro1 was completely lost only for the K105A mutant (Fig. 6 E). To more definitively assess acetylation of K105, we used acetylated Miro1 peptides to generate an anti–Miro1-AcK105 antibody. Anti–Miro1-AcK105 showed a single band on immunoblots of lysates from DRG neurons, with a clear increase in signal when the cells were exposed to TubA (Fig. 6 F). The anti–Miro1-AcK105 signals were completely lost when the immunizing peptide was included with the primary antibody in the immunoblotting procedure (Fig. 6 F). siRNAs to Miro1 decreased signals for anti-Miro1 and anti–Miro1-AcK105, and blocking peptide reduced anti–Miro1-AcK105 immunofluorescent signals in axons (Fig. S6, C and D). Thus, the anti–Miro1-AcK105 antibody is specific for acetylated

Figure 6. **Miro1 K105Q is an axonal substrate for HDAC6 after exposure to CNS growth inhibitors. (A)** End-point FRAP for Mito-GFP recovery in distal axons of DRGs transfected with WT, acetyl-mimetic (K40Q), or nonacetylatable (K40A) α-tubulin constructs and plated onto laminin is shown as average of normalized percentage recovery ± SEM at 960 s after bleach. Exposure to 10 µM TubA significantly increases Mito-GFP recovery in all three conditions (*, P ≤ 0.05 for TubA-treated vs. its corresponding DMSO control by two-way ANOVA with Tukey post hoc). Fig. S6 (A and B) shows that these mutant α-tubulin proteins are incorporated into axonal microtubules and expressed at relatively equivalent levels. **(B)** Representative immunoblot is shown for Miro1 from input and immunoprecipitations with magnetic bead-conjugated nonimmune IgGs or anti–Ac-Lys antibody cocktail from DRG neurons treated with 10 µM TubA for 4 h. 10% of the protein lysate was used as input (pull-down efficiency of 10.1 ± 1.9% for control vs. 14.1 ± 2.2% for TubA over n = 4; P = 0.012 by two-tailed Student's t test). **(C)** HDAC6 is detected in Miro1 immunoprecipitates, and Miro1 is detected in HDAC6 immunoprecipitates from cultured DRG neurons by immunoblotting. 10% of the protein lysate was used as input. **(D)** Schematic of rat Miro1 sequence with residues previously reported to be acetylated in nonneuronal cells indicated (K105, K525, and K629 plus (Ac)). The glutamate-to-lysine mutations that were previously reported to decrease Miro1 Ca²⁺ sensitivity are indicated by (KK). Residues corresponding to GTPase, EF-hand, and transmembrane (TM) domains are shown. **(E)** Representative immunoblots are shown for anti-Myc from DRG neurons transfected with Myc-Miro1^{K105A}, Myc-Miro1^{K525A}, or Myc-Miro1^{K629A} plasmids and treated with 10 µM TubA for 4 h at 36 h after transfection (40 h in vitro). Input (10%) and immunoprecipitations with nonimmune IgG and Ac-Lys antibody cocktail. **(F)** Representative immunoblots are shown for anti–Miro1-AcK105 for DRG lysates ± 10 µM TubA. For the righthand blot, the anti–Miro1-AcK105 antibody was preincubated with 100 µg/ml immunizing peptide (short exposure = 30 s; long exposure = 3 min). **(G and H)** Representative immunoblots are shown in G for anti–Miro1-AcK105, anti-Miro1, and anti-Erk1 (loading control) from lysates of DRG cultures treated with 10 µg/ml aggrecan (CSPG) or 1 µM thapsigargin (Thapsi) for 4 h. H shows quantification of immunoblot signals across multiple experiments as average fold-change relative to control ± SEM (n = 3; *, P ≤ 0.05 by one-way ANOVA with pairwise comparison and Tukey post hoc tests). **(I and J)** Representative confocal projection images (XYZ) for anti-Miro1-AcK105 (Cy5), anti-NF (Cy3), and MitoTracker Green are shown as indicated in J for control, aggrecan-treated (CSPG) or thapsigargin-treated cultures. ImageJ was used for pseudocoloring and channel merging. Panel I shows quantification of the axonal anti-Miro1-AcK105 signals under these conditions as average fold-change relative to control ± SEM (n = 20; *, P ≤ 0.05 by one-way ANOVA with pairwise comparison and Tukey post hoc; scale bar = 20 µm; 100×/1.4 NA objective used).

Miro1 protein. Indeed, exposing DRG cultures to bath-applied aggrecan or increased intracellular [Ca^{2+}] with thapsigargin treatment decreased Miro1-AcK105 overall by immunoblotting (Fig. 6, G and H) and in axons by immunofluorescence (Fig. 6, I and J).

K105 acetylation of Miro1 supports axon growth on nonpermissive substrates and decreases sensitivity of mitochondrial transport to elevated [Ca^{2+}]

Ca^{2+} binding to Miro1's EF-hand (Fig. 6 D) motifs causes its dissociation from motor proteins and attenuates mitochondrial transport (Lee and Lu, 2014). Thus, we considered whether acetylation at K105 might alter Miro1's sensitivity to Ca^{2+}. Replacement of two lysines in Miro1's EF-hand with glutamates (Miro-KK; Fig. 6 D) renders the protein insensitive to this Ca^{2+} effect (Fransson et al., 2006). To test the possibility that Ca^{2+} sensitivity of Miro1 regulates axon growth, we compared responses to aggrecan for DRG neurons transfected with Miro-KK or WT Miro1. Miro-KK expression prevented the decrease in Mito-GFP recovery observed by FRAP assays in distal axons after bath-applied aggrecan (Fig. 7 A). Miro-KK similarly rescued the decrease in ψ_M that was seen in axons of neurons cultured on substrate-bound aggrecan (Fig. 7 B). Consistent with these effects on axonal mitochondria, axon length was significantly greater in Miro-KK–expressing DRGs cultured on aggrecan-coated coverslips (Fig. 7 C). However, similar to HDAC6 inhibition, axon growth was not affected on laminin (Fig. 7 C). These data indicate that Miro1's sensitivity to Ca^{2+}, which determines Miro1's interaction with Milton and mitochondrial association with motor proteins (Lee and Lu, 2014), contributes to the CSPG-dependent decrease in mitochondrial transport, ψ_M, and axon growth.

To directly test how acetylation of Miro1 affects axonal responses to growth-inhibitory substrates, we generated Myc-tagged Miro1 acetyl-mimetic mutants with Gln at K105 and K629 (Myc-Miro1^{K105Q} and Myc-Miro1^{K629Q}, respectively). DRG neurons transfected with each construct showed that the WT and all of the mutant Myc-Miro1 proteins extend into axons and colocalize with mitochondria (Figs. 7 E and S7 A). By FRAP analyses, Myc-Miro1^{K105Q} expression, but not Myc-Miro1 or Myc-Miro1^{K629Q}, prevented the attenuation of mitochondrial transport seen with bath-applied CSPG (Fig. 7 E). For DRG neurons grown on aggrecan-coated coverslips, Myc-Miro1^{K105Q} expression prevented the net shift to a higher proportion of retrogradely moving axonal mitochondria than was seen with expression of Myc-Miro1, acetyl-mimetic Myc-Miro1^{K629Q}, or the nonacetylatable Miro1 K-to-A mutants (Myc-Miro1^{K105A} and Myc-Miro1^{K6298A}, respectively; Fig. 7 F). No significant changes were seen for mitochondrial movements when these neurons were cultured on the permissive substrate laminin, or for speed of transport when cultured on CSPG or laminin substrates (Fig. S7, B and C). Applying aggrecan adsorbed onto microbeads (CSPG-beads) to DRG cultures enabled us to provide a focal source of CSPG exposure to axons versus cell bodies (Willis et al., 2007). Similar to bath application of aggrecan, the CSPG-beads decreased mitochondrial transport in DRG cultures, but only when the beads lay adjacent to axons and not the neuronal cell

body, indicating that this HDAC-dependent change in mitochondrial transport requires axonal signaling (Fig. S7 D). Expression of Myc-Miro1^{K105Q}, but not Myc-Miro1 or Myc-Miro1^{K629Q}, similarly prevented the decrease in mitochondrial transport from axonal CSGP stimulation (Fig. 7 G). Interestingly, Myc-Miro1^{K105Q} expression supported axon growth on aggrecan-coated coverslips for adult DRG neurons that was comparable to the Miro1KK mutant, while no axon growth above control was seen with Myc-Miro1^{K629Q} expression (Fig. 7 H). To directly test whether Miro1 K105 acetylation impacts the protein's sensitivity to elevated [Ca^{2+}], we treated Myc-Miro1^{K105Q}–expressing and Myc-Miro1^{K629Q}–expressing DRGs with thapsigargin to release ER Ca^{2+} stores and assessed mito-GFP transport in distal axons. Axons of the Myc-Miro1^{K105Q}–expressing DRG neurons showed significantly higher Mito-GFP fluorescence recovery than Myc-Miro1^{K629Q}–expressing neurons (Fig. 7 I). The Mito-GFP recovery for thapsigargin-treated cultures was significantly increased by TubA treatment in the Myc-Miro1^{K629Q}–expressing neurons, but Myc-Miro1^{K105Q}–expressing neurons showed only a modest response to TubA treatment (Fig. 7 I).

Discussion

We previously reported that inhibition of HDAC6 supports axon growth on nonpermissive substrates (Rivieccio et al., 2009), suggesting that the substrates of HDAC6 contribute to the growth inhibition from these stimuli. Although HDAC6 has nuclear functions (Verdel et al., 2000), this protein was identified as an α-tubulin deacetylase (Hubbert et al., 2002), and HDAC6 knockout mice show a generalized increase in Ac-α-tubulin levels in all tissues (Zhang et al., 2008). The deacetylation of axonal α-tubulin has generally been interpreted as responsible for HDAC6's effects on axon growth. However, we find that the outer mitochondrial membrane protein Miro1 is a substrate for HDAC6 in axons, with deacetylation of Miro1 K105 decreasing mitochondrial transport in axons and attenuating axon growth in response to CSPGs and MAG. Mitochondria play multiple roles in growing and mature axons by providing a source of ATP for energy needs and serving as a storage site for Ca^{2+} (Smith and Gallo, 2018). Mitochondrial transport and function have been linked directly to axon growth, and Miro1 plays a critical role in kinesin- and dynein-dependent transport of mitochondria by linking these organelles to the motor proteins. Although Miro1's phosphorylation by PINK1 and subsequent ubiquitination by Parkin were shown to attenuate mitochondrial transport by targeting Miro1 for degradation (Birsa et al., 2014; Shlevkov et al., 2016), possible roles for acetylation of Miro1 and its effects on mitochondria have not previously been reported. Moreover, K105 for rat and mouse or K92 for human Miro1 do not correspond to any of the reported Miro1 ubiquitination sites (Kazlauskaite et al., 2014), suggesting that the mechanism for sustaining mitochondrial transport through Miro1 K105 acetylation is unlikely to be a simple prevention of ubiquitination.

The Gallo laboratory recently showed that CSPGs decrease mitochondrial motility in growth cones of chick DRG neurons
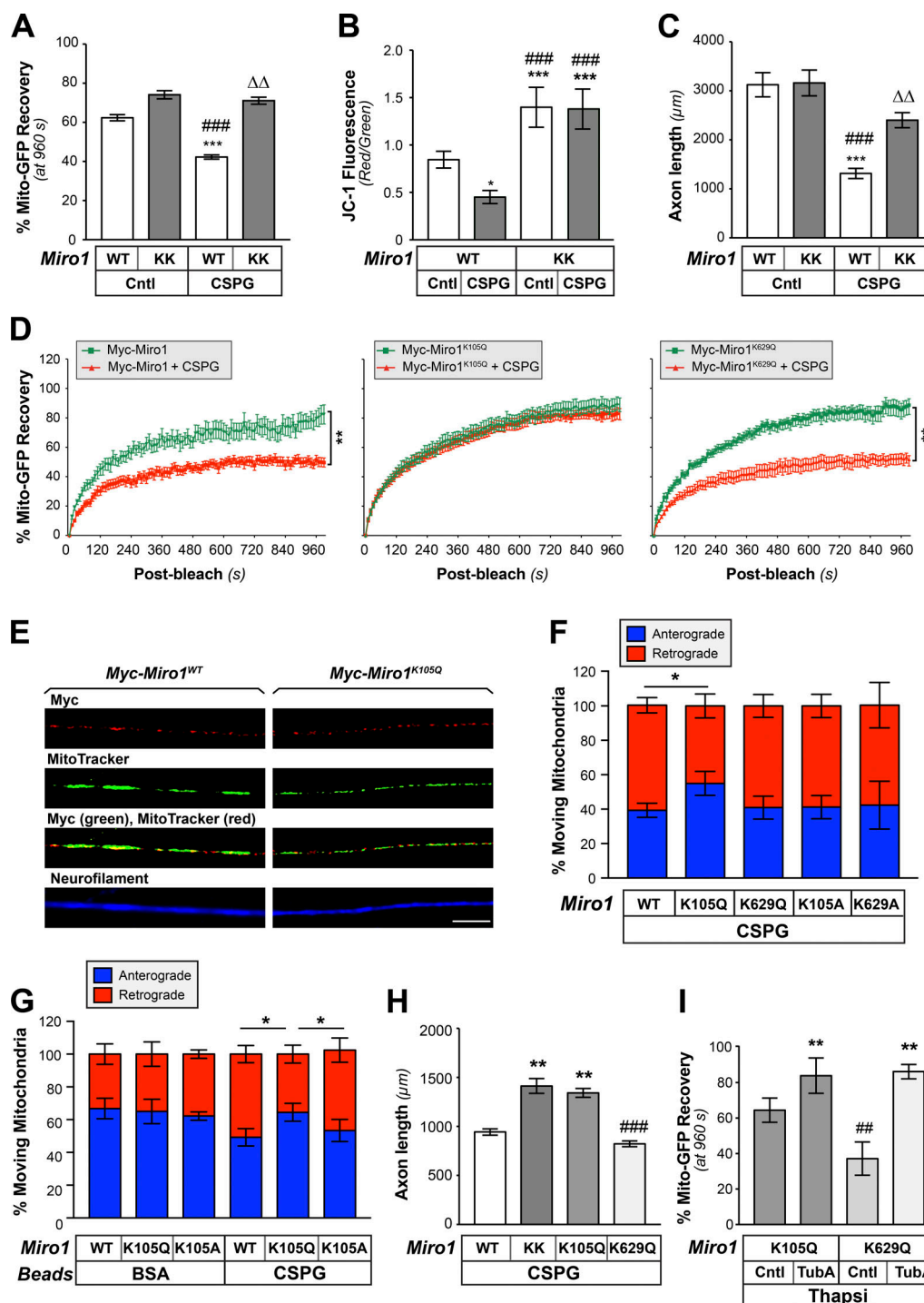
Figure 7. **Acetylation of Miro1 on K105 increases mitochondrial transport and supports axon growth on CNS growth inhibitory substrates. (A)** End-point FRAP analysis for Mito-GFP in distal axons of DRGs transfected with either Myc-Miro1 (WT) or Myc-Miro1KK (KK) plasmids and cultured on laminin ± bath-applied 10 µg/ml aggrecan (CSPG) is shown as average of normalized percentage recovery ± SEM at 960 s after bleach ($n \geq 16$ axons over four culture preparations; ***, $P \leq 0.005$ vs. control + WT; ###, $P \leq 0.005$ vs. control + Miro1KK; $\Delta\Delta$, $P \leq 0.01$ vs. CSPG + WT by two-way ANOVA with Tukey post hoc). **(B)** Miro-KK expression prevents aggrecan-dependent decrease in axonal ψ_M as evidenced by JC-1 fluorescence ratio for DRGs cultured on laminin-coated (Cntl) versus aggrecan-coated (CSPG) coverslips. Average ratio ± SEM is shown ($n = 20$; *, $P \leq 0.05$; ***, $P \leq 0.005$ vs. control; ###, $P \leq 0.005$ vs. CSPG by one-way ANOVA with pairwise comparison and Tukey post hoc). **(C)** DRGs transfected as in B were cultured on laminin (Cntl) or aggrecan (CSPG) substrates. Axon length assessed at 72 h after transfection is shown as average total axon length/neuron ± SEM ($n \geq 95$ each over three DRG cultures; ***, $P \leq 0.005$ vs. control + WT; ###, $P \leq 0.005$ vs. control + Miro-KK; $\Delta\Delta$, $P \leq 0.01$ vs. CSPG + WT as determined by two-way ANOVA with Tukey post hoc). **(D)** FRAP analyses for Mito-GFP in distal axons of DRGs transfected with Myc-Miro1, Myc-Miro1^{K105Q}, or Myc-Miro1^{K629Q} and cultured on laminin and then ± bath-applied 10 µg/ml aggrecan (CSPG) are shown as average normalized percentage recovery ± SEM ($n \geq 9$ axons over three culture preparations; **, $P \leq 0.005$ for indicated treatments by two-way ANOVA with Tukey honestly significant difference [HSD] post hoc). **(E)** Representative immunofluorescent images for Myc-Miro1 or Myc-Miro1^{K105Q}

(FITC) and NF (Cy5) along axons of cultured DRG neurons shows that both proteins localize to axons and colocalize with MitoTracker signals. See Fig. S7 A for Myc-Miro1^{K105A}, Myc-Miro1^{K629Q}, and Myc-Miro1^{K629A} immunofluorescence (scale bar = 10 µm; 100×/1.4 NA objective used). **(F)** Percentage of moving axonal mitochondrial showing anterograde (blue) versus retrograde (red) directions in DRG neurons transfected with indicated Myc-tagged Miro1 constructs and plated on aggrecan (CSPG). Average values ± SEM are shown. See Fig. S7 B for axonal mitochondrial dynamics for these neurons cultured on laminin and Fig. S6 C for analyses of transport speed for laminin and CSPG cultured DRGs (n = 20 axons over three culture preparations; *, P < 0.05 by one-way ANOVA with pairwise comparison and Tukey post hoc). **(G)** Percentage of retrogradely (red) and anterogradely (blue) moving mitochondria in growth cone of rat adult DRG neurons expressing Myc-Miro1^{K105Q} or Myc-Miro1^{K105A} and mito-GFP when axons are exposed to CSPG-coated versus control BSA-coated microspheres. Average values ± SEM are shown; note that Fig. S7 D shows that axonal mitochondrial transport is affected only by axonal exposure to the CSPG microspheres and when presented at the cell body (n = 15 axons over three culture preparations; *, P ≤ 0.05 by one-way ANOVA with pairwise comparison and Tukey post hoc). **(H)** Axon growth on substrate-bound aggrecan (CSPG) for DRGs transfected with Miro1 WT, KK, or acetyl-mimetic mutants (K105Q and K629Q) plasmids is shown as average total axon length/neuron ± SEM. Axon length was assessed at 72 h after transfection (n ≥ 75 each over three DRG cultures; **, P ≤ 0.005 vs. WT; ###, P ≤ 0.001 vs. Miro1KK and Miro1^{K105Q} by two-way ANOVA with Tukey HSD post hoc). Myc-Miro-KK and Myc-Miro1^{K105Q} are not statistically different. **(I)** End-point FRAP is shown for Mito-GFP recovery in distal axons of DRGs transfected with either Miro1 K105Q or K629Q plasmids and cultured on laminin followed by treatment with 1 µM thapsigargin plus vehicle control (DMSO), or 10 µM TubA is shown as average of normalized percentage recovery ± SEM at 960 s after bleach (n ≥ 16 axons over four culture preparations; **, P ≤ 0.01 vs. Miro1^{K105Q} control or Miro1^{K629Q} control; ##, P ≤ 0.01 vs. Miro1^{K105Q} + TubA by two-way ANOVA with Tukey HSD post hoc).

(Sainath et al., 2017), and our data extend this to show that both MAG and CSPGs decrease mitochondrial transport and membrane potential in adult rat sensory axons. Moreover, we show that this alteration in mitochondrial motility is through a localized, axon-intrinsic mechanism that is overcome by expression of acetyl-mimetic Miro1. CNS growth inhibitors block axon growth in part through activating RhoA that is known to cause F-actin depolymerization (Fujita and Yamashita, 2014). These growth inhibitors are also known to increase intracellular Ca^{2+} (Snow et al., 1994; Henley et al., 2004). Activation of RhoA has been shown to trigger release of intracellular Ca^{2+} stores in fibroblasts (Lee et al., 1998), but it was not known if this occurs in neurons. By using a combination of a pharmacological RhoA activator, ROCK inhibitor, Ca^{2+} chelator, and sarco/ER Ca^{2+}-ATPase (SERCA) inhibition, our data indicate that activation of RhoA by CSPG and MAG increases intracellular Ca^{2+}, with a subsequent Ca^{2+}-dependent activation of HDAC6 to deacetylate Miro1. The acetyl-mimetic Miro1^{K105Q} prevents the decrease in mitochondrial transport and ψ_M after CPSG exposure, by direct activation of RhoA and by direct elevations of cytoplasmic Ca^{2+} through SERCA inhibition. Taken together, these functions for HDAC6 and Miro1-AcK105 downstream of CSPGs and MAG provide new mechanistic insight into axon-intrinsic effects of these CNS growth inhibitors beyond their effects on cytoskeleton.

The attenuation of mitochondrial transport seen with MAG and CSPG exposure is clearly Ca^{2+} dependent, since Ca^{2+} chelation with BAPTA-AM prevented the decrease in mitochondrial trafficking seen with these stimuli. Ca^{2+}-binding to Miro proteins' EF-hands triggers release of mitochondria from kinesin interaction to attenuate anterograde mitochondrial transport (Saxton and Hollenbeck, 2012). The Miro/Milton complex also contributes to dynein-dependent mitochondrial transport (van Spronsen et al., 2013), so Ca^{2+} binding to Miro could also affect retrograde mitochondrial transport. Consistent with this, Mito-GFP FRAP analyses on axon shafts show that MAG attenuated both anterograde and retrograde mitochondrial transport in axons. The link between increased axoplasmic Ca^{2+} after exposure to CNS growth inhibitors and the decreased mitochondrial transport is supported by our experiments with the Ca^{2+}-resistant form of Miro1. This Miro-KK mutant prevented the CSPG-dependent decrease in axonal mitochondrial transport and ψ_M,

as well as supported axon growth on aggrecan. The acetyl-mimetic Miro1^{K105Q} equally rescues the effects of CSPGs on mitochondrial transport, ψ_M, and axon growth. This indicates that acetylation on K105 could contribute to Miro1's Ca^{2+} sensitivity or binding. Consistent with this, Miro1^{K105Q} protected decrease in mitochondrial transport and ψ_M when axoplasmic Ca^{2+} was directly increased by inhibiting SERCA with thapsigargin. K105 is within Miro1's N-terminal GTPase domain rather than the Ca^{2+} binding EF-hands. This domain of Miro1 is needed for both kinesin- and dynein-dependent mitochondrial transport in cortical neurons (Babic et al., 2015). Future work will be needed to determine if K105 acetylation alters the GTPase activity of Miro1 and how this might affect Ca^{2+} binding/sensitivity of Miro1's EF-hands. Miro 1 has recently been shown to interact with mitochondrial Ca^{2+} uniporter protein, and this is needed for Miro1-dependent transport of mitochondria (Niescier et al., 2018). The balance of Ca^{2+} levels in the mitochondrial matrix is needed for mitochondrial transport, as increased mitochondrial Ca^{2+} generated through mitochondrial Ca^{2+} uniporter attenuates mitochondrial transport (Chang et al., 2011). With Miro1^{K105Q} preventing both the decrease in mitochondrial transport and ψ_M seen after treatment with thapsigargin, it is intriguing to speculate that the acetylation status of Miro1 may also help determine Ca^{2+} levels in the mitochondrial matrix.

Mitochondria are the major source of ATP for the axon and play a critical role in Ca^{2+} buffering (Lin and Sheng, 2015). Mitochondrial trafficking in axons has been linked to developmental growth of retinal ganglion cell (RGC) neurons, and increased axonal mitochondrial content correlated with increased developmental and regenerative growth capacity (Steketee et al., 2012; Cartoni et al., 2017). Mitochondrial motility in axons of cortical neurons progressively declines as their axons mature during development (Lewis et al., 2016). Expression of Syntaphilin, which provides Ca^{2+}-dependent docking of mitochondria along axons, increases with neuronal maturation, and depletion of Syntaphilin increases axon regeneration rates in the peripheral nervous system (PNS; Zhou et al., 2016). In contrast to the PNS, mature RGC axons in the optic nerve have low spontaneous regeneration and need to be coaxed to regenerate by activating growth programs exogenously (Benowitz et al., 2017). When optic nerve regeneration is activated by

deletion of the phosphatase and tensin homolog, there is a commensurate increase in the mitochondrial protein Armcx1 that results in increased transport of mitochondria in RGC axons (Cartoni et al., 2016). Differences in the extracellular environment of the injured CNS versus PNS are one of the factors that allow PNS neurons to spontaneously regenerate. Thus, the rapid decrease in axonal mitochondrial motility that we see in the PNS neurons used here after exposure to MAG and CSGP likely contributes to the axon growth inhibition.

Inhibition of HDAC6 has been suggested as potential therapeutic intervention for neuropathic conditions. Axon degeneration from chemotherapy agents vincristine and cisplatin was prevented by pretreatment with HDAC6 inhibitors (Krukowski et al., 2017; Van Helleputte et al., 2018), and HDAC6 inhibition was shown to reverse axon transport deficits in Charcot Marie Tooth 2 neuropathy models caused by HSPB1 mutation and glycyl tRNA synthetase (GlyRS) mutations (d'Ydewalle et al., 2011; Benoy et al., 2018). In each of these models, axon protection was accompanied by an increase in Ac-α-tubulin levels, suggesting that the protective mechanism is through stabilization of microtubules. Indeed, the mutant GlyRS was shown to interact with HDAC6 and stimulate its activity to decrease Ac-α-tubulin levels (Mo et al., 2018). However, mitochondrial transport is also altered in many neuropathic disorders (Pareyson et al., 2015). Mitochondrial trafficking in axons also decreases in Alzheimer's and Huntington's disease models, and inhibition of HDAC6 can overcome these deficits (Dompierre et al., 2007; Kim et al., 2012), raising the possibility that the acetylation/deacetylation status of Miro1 may also contribute to neurodegeneration. Reversal of mitochondrial trafficking defects in axons of human stem cell–derived motor neurons expressing amyotrophic lateral sclerosis–causing FUS protein mutants has also recently been reported (Guo et al., 2017). Ac-α-tubulin is associated with stabilized microtubules (Cambray-Deakin and Burgoyne, 1987; Baas and Black, 1990), which has been shown to provide preferential binding for Kinesin-1 (Ertürk et al., 2007) that could effectively increase anterograde transport of mitochondria and other cargoes. However, our data show that acetylation of Miro1 on K105 results in increased movement of mitochondria in axons. This raises the distinct possibility that increased acetylation of Miro1 contributes to the protective effects of HDAC6 inhibitors in neuropathic and neurodegenerative disorders.

It should be noted that Lin et al. (2015) reported that inhibition of HDAC6 could attenuate axon growth on permissive substrates. They also reported that axon crossing from permissive (laminin) to nonpermissive (CSPG) substrates was decreased by inhibition of HDAC6 (Lin et al., 2015), which conflicts with our observations using bath-applied and substrate-bound aggrecan as well as with our previous work (Rivieccio et al., 2009). Differences in presentation of the inhibitory substrates may explain this discrepancy. Axons crossing a CSPG border as used by Lin et al. (2015) are indeed different from the soluble and CSPG-coated coverslips used here. Interestingly, the adult DRG cultures used here showed decreased axon growth in escalating gradients of CSPGs ("spot assays"; Tom et al., 2004) that was not prevented by HDAC6 inhibition (not depicted) Thus,

there may be different axonal responses based on how the nonpermissive stimulus is presented. Nonetheless, our data emphasize that the effects on axon growth and mitochondrial transport are generated from signals within the axons.

In summary, the work here shows that CNS growth inhibitors decrease mitochondrial transport in axons through an axon-intrinsic mechanism that is HDAC6 dependent and results in deacetylation of Miro1 K105. Acetyl-mimetic Miro1^{K105Q} mutant supports growth on these growth inhibitors and prevent decreases in mitochondrial transport and ψ_M seen after exposure. CSPGs were also recently shown to impair mitochondria/ER targeting into growth cones of embryonic chick sensory neurons, with an accompanying decrease in ψ_M (Sainath et al., 2017). This targeting deficit was suggested to disrupt functional linkages between mitochondria and ER. Mitochondrial-associated ER membranes facilitate Ca^{2+} and phospholipid exchange between the two organelles and contribute to their trafficking, including transport in axons (Paillusson et al., 2016). Disrupted mitochondrial trafficking and axonal mitochondrial-associated ER membranes were recently reported on expression of an amyotrophic lateral sclerosis–causing mutant of FUS in neurons (Guo et al., 2017). The altered Ca^{2+} sensitivity of acetylated Miro1 raises the possibility that Miro1-Ac-K105 could impact the interactions of mitochondria with ER in axons. It is not clear which protein acetylates Miro1. As noted, we recently showed that αTAT1 is destabilized by activation of RhoA/ROCK signaling, and overexpression of αTAT1 supports axon growth on the nonpermissive substrates used here (Wong et al., 2018). Further work will be needed to determine if αTAT can acetylate Miro1, but our data clearly indicate that the balance of Miro1 acetylation and deacetylation can help to drive axon growth on nonpermissive substrates.

Materials and methods

Animal care and use
All vertebrate animal experiments were performed under protocols approved by Institutional Animal Care and Use Committees of Drexel University, University of South Carolina, University of Michigan, Weill Cornell Medicine, or University College London–Institute of Neurology Ethics Committee under license from the UK Home Office in accordance with the Animals (Scientific Procedures) Act (1986). Male Sprague-Dawley rats (175–250 g) or female C57BL/6 mice (6–8 wk) were used for all experiments. Animals were killed using CO_2 asphyxiation per approved methods. L4-5 DRGs were rapidly removed for dissociated culture (see below).

For in vivo inhibition of HDAC6, the sciatic nerve of anesthetized adult rats was injected twice at mid-thigh level with 2 μl of 1.5 mM TubA on the right and 2 μl of DMSO (vehicle control) on the left (isofluorane inhalation was used for anesthesia). Nerve injection sites were separated by 2 mm. Animals were used for in vivo imaging of mitochondrial transport or killed 2 h after injection for harvesting sciatic nerves for EM analyses.

Primary neuron cultures
For primary culture of rat DRG neurons, L4-5 DRG were harvested in Hibernate-A medium (BrainBits) and then dissociated

using type I collagenase (50 U/ml; Gibco) for 20 min at 37°C and 5% CO_2 (Twiss et al., 2000). Dissociated ganglia were cultured in complete medium containing 10% FetalPlex animal serum complex (Gemini), 1% N1 Supplement (Sigma-Aldrich), and 10 µM cytosine-arabinoside (Sigma-Aldrich) on laminin/poly-L-lysine–coated substrates. Mouse neurons were used for cultures in microfluidic devices. For these, all cervical, thoracic, and lumbar DRGs were collected and digested with collagenase (4 mg/ml, Worthington) and dispase (1 mg/ml; Sigma-Aldrich) for 45 min at 37°C and 5% CO_2; these cells were plated in DMEM/F12 and 10% FBS at 37°C and 5% CO_2.

18–24-h DRG cultures were used for immunostaining and MitoTracker experiments. For transfection, neurons were cultured for 72 h after nucleofection and plating. DRGs were cultured on glass coverslips for immunostaining, glass-bottom 35-mm dishes (Wilco) for live-cell imaging, or microfluidic devices for selective treatment of axonal processes.

For inhibition of HDAC6, DRG cultures were treated with TubA (10 µM, reconstituted in DMSO; Rivieccio et al., 2009) for indicated durations. The same final concentration of DMSO was added to control cultures for all TubA experiments ("vehicle control"). MitoTracker Green (Invitrogen; M7514) was used to visualize mitochondria in DRG cultures; this was prepared according to manufacturer's instructions and used at 50 nM applied 30 min before imaging followed by two washes in fresh medium.

MAG or Aggrecan exposures were performed as bath application or on coated substrates. For bath application, dissociated DRGs were cultured for 48 h and treated with 25 µg/ml of MAG-Fc (R&D Systems; 538-MG), 25 µg/ml Fc control (R&D Systems; 110-HG), or 10 µg/ml of Aggrecan (Sigma-Aldrich; A1960) for 4 h. Cultures were pretreated with either Ca^{2+} chelator BAPTA-AM (3 µM; Sigma-Aldrich; A1076), ROCK inhibitor Y27632 (10 µM; Sigma-Aldrich; SCM075), HDAC6 inhibitor TubA (10 µM; R&D Systems; 6270), Thapsigargin (1 µM; Sigma-Aldrich; T9033), Rho Activator II (1 µg/ml; Cytoskeleton; CN03), or equivalent volume DMSO 30 min before MAG-Fc, Aggrecan, or controls. For substrate-bound experiments, adult DRGs were cultured on glass bottom dishes (Greiner) that were coated with 25 µg/ml Aggrecan in addition to the laminin/poly-D-lysine substrate.

For microfluidic experiments, adult mouse DRG neurons were cultured in compartmentalized chambers (Xona Microfluidics) to separate axons from cell bodies. Dissociated ganglia were seeded in the cell body compartment at a high density of 5×10^5 cells/10 µl until high axon density was observed in the axonal compartment (≥42 h). TubA or DMSO was then applied to the axonal compartment with and without preincubation with MAG (25 µg/ml) for 4 h. Mitochondria were labeled with MitoTracker Green (50 nM) as above.

DNA constructs and transfections

Mito-GFP construct (pABCb10aa1-35-GFP; Addgene) was used as a mitochondrial marker (Graf et al., 2004). pMito-KR (Evrogen) was used to ablate mitochondria in growth cones and in some cases as a mitochondrial marker. Transfection with pTagBFP (Evrogen) was used to visualize axons and growth cones. The

Myc-tagged Miro1 (WT) and Myc-Miro1$^{E208K/E328K}$ (Miro-KK) expression constructs were purchased from Addgene (plasmid 47888 and 47894, respectively). Quikchange site-directed mutagenesis kit (Agilent; 200521) was used to introduce point mutations into the Myc-Miro1 WT plasmid to generate the nonacetylatable (K to A) and acetyl-mimetic (K to Q) constructs. mCherry-tagged α-tubulin expression plasmids (WT, nonacetylatable K40A, acetyl-mimetic K40Q) were previously described (Lee et al., 2015).

DRG cultures were transfected using the Amaxa Nucleofector with basic neuron SCN Nucleofector Kit (Lonza) and analyzed by live-cell imaging 48–72 h later. SiRNAs for HDAC6 have been described previously (Rivieccio et al., 2009); these were transfected with DarmaFect3 (Dharmacon), and cells were analyzed in live-cell imaging as above. siRNAs used for Miro1 knockdown were: #1, 5′-CAACAAACAUUCUAUUGAUAAGGTA-3′, and #2, 5′-CCUGCAUGAAGUCAAGCAAGAACAC-3′ (Integrated DNA Technologies).

Generation of anti–Miro1-AcK105 antibody

Anti–Miro1-AcK105 polyclonal antibody was generated in rabbits by ProSCI. After collection of preimmune serum, each rabbit was immunized at 0, 2, and 4 wk with the rat Miro1 (SwissProt accession no. NP_001100496.1) Ac-Lys peptide, KHSIDK(Ac)VTSR (K105 in rat is corresponds to human K92), in complete Freund's adjuvant. Rabbits were boosted once intramuscularly at week 6 with peptide formulated in incomplete Freund's adjuvant. Bleeds were collected at weeks 5 and 7 for serum isolation and testing.

Antisera were initially tested using ELISA with all steps at room temperature and incubations in humidified chambers. For this, peptides, KHSIDK(Ac)VTSR versus KHSIDKVTSR (10 µg/ml per well in 100 µl of 50 mM carbonate buffer), were conjugated to 96-well plates. After 24-h incubation, plates were washed five times with distilled water and incubated for 2 h in blocking buffer (200 µl of 1% BSA and 0.02% thimerosal in PBS). Plates were washed twice with distilled water. 100 µl of serially diluted preimmune and immune sera in blocking buffer was added to wells (duplicate wells) for 2 h. Plates were washed three times using blocking buffer followed by three washes with distilled water. Each well was incubated with 100 µl of HRP-conjugated anti-rabbit secondary antibody diluted in blocking buffer for 2 h. Plates were washed five times with blocking buffer, followed by five washes with distilled water. Plates were developed for 10 min in 100 µl of a 3,3′,5,5′-tetramethylbenzidine substrate solution. The reaction was stopped with 50 µl of 1 N HCL, and absorbance at 450 nm was read on a plate reader.

For affinity purification, an immune-affinity chromatography column (5 ml) was prepared by cross-linking the KHSIDK(Ac)VTSR peptide to CNBr-activated sepharose 4B. Immune serum was centrifuged and filtered through a 0.45-µm filter. The immune-affinity purification column was washed with 50 ml of PBS. 5 ml serum was added, column ends were capped, and the column was rotated for 30 min. Caps were removed from the column to drain the serum, and the process was repeated until the rest of the serum was passed through the column. The column was washed with 50 ml of PBS; bound

antibody was eluted with 100 mM glycine buffer, pH 2.5; and 1-ml fractions were collected into tubes containing 50 µl of 1 M Tris, pH 9.5. The fractions containing the antibody were pooled, and the antibody was dialyzed using 12–14-kD dialysis tubing against three changes of PBS. NaN$_3$ was added to the concentrated antibody solution for preservative (at 0.025%).

Immunoprecipitation

DRG neurons were lysed in 100 mM KCl, 5 mM MgCl$_2$, 10 mM Hepes, pH 7.4, 1 mM DTT, and 0.5% NP-40 supplemented with 1× protease inhibitor cocktail (Roche). The lysates were passed through a 25-gauge needle five times and cleared by centrifugation at 12,000 g for 20 min. Equal amounts of the supernatants were then incubated with primary antibodies overnight, and immunocomplexes were precipitated with Protein G–Dynabeads (Invitrogen) for an additional 2 h at 4°C with rotation. A cocktail of rabbit and mouse anti–Ac-Lys antibodies (5 µg each; Cell Signaling; 9441 and 9681) was used directly for analyses of Myc-Miro1 transfected cultures by immunoprecipitation. For analysis of endogenous Miro1 acetylation, the anti-Lys antibody cocktail (5 µg of each) was directly cross-linked to 5 mg of M-270 epoxy beads (Dynabeads) using the Dynabeads antibody coupling kit according to the manufacturer's instructions (Life Technologies; 14311D). 100 µg of cleared lysates from DRG cultures were then incubated with the beads overnight at 4°C with rotation. Beads were washed five times with cold lysis buffer, and immunocomplexes were released by boiling in Laemmli sample buffer and processed for immunoblotting as below.

Immunoblotting

For immunoblotting, protein lysates or immunoprecipitates were denatured by boiling in Laemmli sample buffer, fractionated by SDS-PAGE, and transferred to nitrocellulose membranes. Blots were blocked for 1 h at room temperature with 5% nonfat dry milk in TBS with 0.1% Tween 20 (TBST). Primary antibodies diluted in 5% BSA in TBST were added to the membranes and incubated overnight at 4°C with rocking. Primary antibodies consisted of rabbit anti-Myc (1:2,000; Cell Signaling; 71D10), rabbit anti-RHOT1 antibody (1:1,000; Aviva Systems Biology; ARP44817_P050), rabbit anti-HDAC6 antibody (1:2,000; Cell Signaling; 7558), rabbit anti-ERK1 (1:5,000; Abcam; ab32537), and affinity-purified custom rabbit anti–Miro1-AcK105 (1:2,500; Twiss laboratory, see above) antibodies. For the anti–Miro1-AcK105 antibody, preimmune and test-bleed sera were used at 1:1,000 dilutions to initially evaluate for specificity. After washing in TBST, blots were incubated with HRP-conjugated anti-rabbit IgG antibodies (1:5,000; Jackson Immunoresearch) diluted in blocking buffer for 1 h at room temperature. Signals were detected using ECL Prime (GE Healthcare) after extensive washing.

Immunofluorescence

Standard immunofluorescence methods were used as previously described (Merianda et al., 2009) at room temperature unless specified otherwise. Briefly, coverslips were rinsed in PBS, fixed in buffered 3.7% PFA for 15–20 min, and washed twice in PBS. Cultures were permeabilized with PBS plus 0.3% Triton X-100

(PBST; Sigma-Aldrich) for 5 min. Coverslips were blocked in 2% BSA and 2% FBS (Gemini) for 1 h. Coverslips were then incubated in the following primary antibodies overnight at 4°C in 1% blocking buffer (Roche): chicken anti-NF cocktail (1:1,000; Aves Lab; NFH, NFM, NFL), rabbit anti-HDAC6 antibody (1:200; Abcam; Ab12173), mouse anti–Ac-α-tubulin IgG (6-11-B1; Sigma-Aldrich; T7451), mouse 9B11 anti-myc (1:1,000; Cell Signaling; 2276), rabbit anti-Myc (1:300; Cell Signaling; 71D10), anti-Miro1 (1:200; Aviva Systems Biology; ARP44817_P050), and custom affinity-purified rabbit anti–Miro1-AcK105 (1:300; Twiss laboratory). After washes in PBST, coverslips were incubated with combinations of FITC-conjugated donkey anti-mouse IgG, Cy5-conjugated donkey anti-chicken IgG, and Cy3-conjugated donkey anti-rabbit IgG (1:200; Jackson Immunoresearch), for 1 h, and then washed twice with 1× PBS, rinsed with distilled H$_2$O, and mounted with Prolong Gold Antifade with DAPI (Life Technologies).

We used a sequential immunostaining approach for simultaneous detection of tyrosinated α-tubulin (by indirect immunofluorescence), Ac-α-tubulin, and β-tubulin (by direct immunofluorescence). Phalloidin staining was also used to detect F-actin. Monoclonal mouse anti–Ac-α-tubulin IgG (6-11-B1; Sigma-Aldrich; T6793) was conjugated to Alexa Fluor 405 using the Zenon Labeling Kit per the manufacturer's instructions (Life Technologies; Z-25013). After fixation and permeabilization, coverslips were incubated with anti–Tyr-α-tubulin IgG (1:100; Sigma-Aldrich; T9028) in 1% blocking buffer overnight at 4°C in a humidified chamber. Cells were washed three times in PBST and then incubated with Cy5-conjugated anti-mouse IgG (1:200; Jackson Immunoresearch) in 1% blocking buffer for 1 h. Cells were washed twice with PBST and then incubated with the Alexa Fluor 405–conjugated mouse 6-11-B1 anti–Ac-α-tubulin (1:50; Sigma-Aldrich; T6793) and FITC-conjugated Tub 2.1 mouse anti–β-tubulin IgG (1:50; Sigma-Aldrich; T4026) in 1% blocking buffer for 1.5 h. Coverslips were washed twice with PBS then stained with Actin-Red 555 Ready Probe for 30 min (1:25 dilution of 200 U/ml stock; Thermo Fisher Scientific; R37112). After rinsing with PBS and then distilled H$_2$O, coverslips were mounted with Prolong Gold Antifade. Signals for tubulin and F-actin were verified as axonal by matching to channels merged with differential interference contrast (DIC) images.

All imaging of immunolabeled samples was performed at room temperature. Epifluorescence and confocal imaging was used for imaging of fixed samples to obtain protein localization and quantitation data. Immunofluorescence and DIC were performed on a Leica DMI6000 M microscope fitted with a Hamamatsu ORCA R2 CCD camera (Hamamatsu) for epifluorescence; Leica HC PL Apo 63×/1.4 NA oil-immersion objectives were used for high-resolution imaging. Images were matched for acquisition parameters using Leica LAS-X software. Confocal imaging for immunofluorescence and DIC were performed on a Leica SP8X microscope (Leica DMI6000 M platform) fitted with a galvanometer Z stage and HyD detectors; HC PL Apo 63×/1.4 NA and HCX PL Apo 100×/1.4 NA objectives (both oil immersion) were used with acquisition parameters matched for individual experiments using LAS-X software. For some experiments as indicated in the figure legends, confocal images were deconvolved using the

Leica Lightning software module. LAS-X software was used to generate XYZ projection images where indicated in figure legends. Both epifluorescent and confocal images were acquired in monochrome; ImageJ (National Institutes of Health) was used for pseudocoloring, channel merging, and image cropping where indicated.

For neurite outgrowth experiments, NF immunofluorescence and DIC imaging were performed with the Leica DM6000 M microscope as above (HCX PL FL 20×/0.50 NA objective; Fig. 1 A) or ImageXpress Micro high content imaging system (Molecular Devices) with Nikon Plan Fluor 10×/0.3 NA objective Photometrics Coolsnap HQ CCD camera (Fig. 4, D and F; and Fig. 7, C and H). Leica LAS-X acquisition software was used for merging tile scans into montage images from the DM6000 M microscope, and MetaExpress software was used for acquiring imaging and merging montage images on the ImageXpress Micro system.

EM

Sciatic nerves were fixed in 2% PFA and 2% glutaraldehyde in PBS overnight and then transferred to PBS. Sciatic nerve segments (±2 mm from injection site) were next processed for ultrastructural studies. The nerve segments were immersed in 1% solution of osmium tetroxide, dehydrated in a graded series of ethanol, and embedded in plastic resin using the Eponate 12TM Kit (Ted Pella). 0.5-µm-thick transverse sections from each nerve segment were cut and stained with toluidine blue for light microscopy. 60–90-nm-thick ultrathin sections were then cut using an RMC Products PowerTome ultramicrotome (Boeckeler Instruments) and collected using formvar-coated one-hole copper grids. All sections were contrasted using uranyl acetate and lead citrate solutions. The ultrathin sections were imaged using a JEOL 100CX transmission electron microscope.

Imaging and analyses of in vivo axonal mitochondria transport

Sciatic nerves were exposed in live, isofluorane-anaesthetized animals (female C57BL6/J mice aged 41–42 d after birth) as previously reported (Gibbs et al., 2016; Sleigh and Schiavo, 2016). Briefly, 10-µl glass micropipettes (Drummond Scientific; 5-000-1001-X10) were pulled (Mohan et al., 2015) and used to inject 2 µl of 1.5 mM TubA or DMSO (Sigma-Aldrich; D2650) vehicle control in sterile saline (0.9% wt/vol) into the proximal aspect of the exposed sciatic nerve. 2 µM tetramethylrhodamine, ethyl ester, perchlorate (Thermo Fisher Scientific; T669), and 0.1% (wt/vol) bromophenol blue (Sigma-Aldrich; B5525) were included in the injected solution to label mitochondria and confirm successful injection beneath the perineurium, respectively. Body temperature was maintained using a heat pad during surgery and drug incubation. Sciatic nerves were imaged from 20 to 90 min after injection using an inverted LSM 780 laser scanning microscope (Zeiss) Plan-Apochromat 63×/1.4 NA Oil DIC M27 objective within an environmental chamber prewarmed and set to 37°C. An area containing labeled axons was selected and imaged for 444–1,000 s at 100× digital zoom every ~4 s (1,024 × 1,024 pixels, 0.5-µs pixel dwell time, 1% laser power). Four animals were imaged per day (two per treatment). Image series were converted into AVI files, and mitochondrial dynamics were assessed using Kinetic Imaging Software. Mitochondria were included in analyses when they could be tracked for at least five consecutive frames. At least 10 mitochondria (mean of 49.1) across at least three axons (mean of 4.38) per animal were tracked, and all analyses were performed blinded to treatment.

Live-cell imaging

All time-lapse experiments on cultured neurons were imaged in complete medium (without phenol red) at 37°C, 5% CO_2, throughout the imaging sequences. Imaging was performed with Leica SP8X confocal microscope as above, with HC PL Apo CS2 40×/1.3 NA or HC PL Apo 63×/1.4 NA oil-immersion objectives and Leica LAS-X software for acquisition, for all experiments except those in Fig. S5 D and the ψ_M analyses. A Leica LAS-X FRAP module was used for acquisition and initial analyses of FRAP image sequences. Temperature and CO_2 were maintained using an environmental enclosure for the DM 6000 M platform. Microscope pinhole was set to 3 Airy units to ensure full-thickness laser exposure to the axon and acquisition of fluorescent emissions. A Zeiss Axio Observer.Z1 microscope fitted with Zeiss Axiocam 503 Mono camera was used for the microfluidic chambers analyzed in Fig. S5 D. An HL PL Apo 63×/1.4 NA oil-immersion objective was used with Zeiss Zen Blue software for acquisition. For ψ_M analyses in cultured neurons, an ImageXpress Micro microscope was used as described above. ImageJ was used for pseudocoloring, channel merging, and cropping of images where indicated.

For mitochondrial motility assays in cultured neurons, L4-5 DRG cultures were incubated with MitoTracker Green as above; ROIs were then scanned every 10 s over 10 min. In some experiments, the same cells were imaged before and after addition of TubA. For this, no DMSO was added to control cultures (i.e., baseline imaging) to avoid doubling the DMSO concentrations with TubA exposure. Potential effects of DMSO were assessed in separate plates from the same culture experiment.

For localized treatment of DRG axons with CSPGs, we used aggrecan-coated microspheres as previously described (Willis et al., 2007). Briefly, 10 µg/ml of Aggrecan (Sigma-Aldrich) was adsorbed to 4.5 µm Carboxylate Microspheres according to the manufacturer's instructions (Polysciences). Microspheres loaded with equivalent concentrations of BSA were used as controls. Microspheres were added to 36-h DRG cultures transfected with Mito-GFP. For time-lapse imaging, growth cones were selected in which microspheres were present within 10 µm. As a control, we selected neurons in which microspheres were present within 10 µm of the cell body, but no microspheres showed in the vicinity of the axon being imaged. Mitochondrial dynamics were monitored by confocal microscopy as above.

For mitochondrial ablation by CALI, DRG cultures expressing Mito-KR and BFP for 48 h were imaged with the same confocal microscope. Mito-KR was activated with an argon laser at 514 nm continuously for 30 s until there was no detectable signal (100% laser power). After activation, 50 µm of the distal axon shaft and the growth cone were imaged every 30 s over 16 min using 585- and 405-nm laser lines (13 and 15.3% power, respectively).

Mito-KR– and Mito-GFP–expressing DRG neurons were used for FRAP analyses at 48–72 h after transfection. To evaluate mitochondrial motility in Mito-KR–expressing neurons, Mito-KR signals were photobleached using continual exposure to an argon laser set at 594 nm for 30 s (100% laser power) The bleached ROI was then monitored for recovery using an argon laser set at 580 nm every 10 s over 16 min (13% laser power). For FRAP analyses with Mito-GFP, GFP signals were photobleached in a 50 μm ROI using an argon laser set at 488 nm every 10 s for 16 min (70% laser power). The same excitation was used for post-bleach imaging to assess recovery every 10 s for 16 min. For axon shaft FRAP experiments in Mito-GFP–expressing neurons, ROIs of ~50 μm in length (without branches) were imaged ≥100 μm proximal to the growth cone. Prebleach, bleach, and post-bleach sequences were the same as for Mito-GFP above. In all cases, neurons were imaged over 40 s or more to acquire baseline Mito-KR or Mito-GFP signals before photobleaching using an argon laser (580 nm at 13% power for Mito-KR and 488 nm at 31% power for Mito-GFP).

JC-1 (Life Technologies) was used for ψ_M measurements. For this, DRG cultures were equilibrated in culture medium with 3 mM JC-1 for 20 min at 37°C. Medium was replaced, and the cells were maintained at 37°C in the high-content imaging system on which JC-1 fluorescent signals in green and red wavelengths were acquired. MetaExpress software (Molecular Devices) was used for image acquisition and generation of montage images.

Image analyses

NF-stained cultures were used for neurite growth analyses. Only neurites ≥100 μm were considered in these analyses from randomly acquired tile scans using WIS-Neuromath (Rishal et al., 2013). Growth cones were distinguished by visualizing the termination of the compacted, parallel, NF-positive bundles in the distal axon shaft by immunofluorescence and by formation of distinct lamellipodia characteristic of the proximal growth cone from DIC images. The growth cone area was measured using ImageJ software from these annotated DIC images. For axon growth in the transfection experiments, images of 72-h DRG cultures were acquired using the ImageXpress Micro system. Axon morphology was visualized NF immunofluorescence, and transfected neurons were identified using Myc immunofluorescence.

Quantification of growth cone mitochondria was performed using high-magnification images from living neurons transfected with either Mito-KR or incubated with MitoTracker. The growth cone was identified by bright-field or DIC images. In the case of MAG-treated cultures in which axons showed retraction, the end bulbs were used for quantification. Only mitochondria that could be distinguished as a single mitochondrion were counted; if this was not possible, that growth cone was not included in the analysis. These measurements were performed by a blinded observer.

Vesicle trafficking was quantified using differential ImageJ Difference Tracker Plug-in (Andrews et al., 2010). 50–80-μm-long unbranched axon segments at approximately the midregion between growth cone and cell body were analyzed. Kymographs were generated using ImageJ Kymograph Plug-in. For analyses

of axon retraction in the CALI experiment, the distance from the distal tip of the growth cone in the pre-CALI image sequence was used as the baseline (t = –1 min). The distance between the growth tip at end of the post-CALI sequence and the pre-CALI baseline was measured using LAS-X software. Movement of ≥0.5 μm toward the axon shaft was counted as retracted. Fluorescence emission of the Mito-KR post-CALI was analyzed using ImageJ. For normalizing intensities across FRAP image sets, fluorescence intensity at each time point was scaled using the LAS-X FRAP module so that the residual fluorescence signal at t = 0 min (post-bleach) was set at 0 and the prebleach intensity was set at 100% for each bleached ROI. For axon shaft FRAP analyses, each 50-μm bleached ROI was divided into four equal 10-μm bins, and the fluorescence intensity recovery was measured as described above.

EMs at 1,900× and 4,800× magnification across the cross-sectional surface of each sciatic nerve were used for in vivo analyses of mitochondrial content. A minimum of 75 unmyelinated axons was analyzed for each nerve. All unmyelinated axons from each analyzed image were included for quantitative studies. The total number of mitochondria was determined in each unmyelinated axon in the field and was divided by the total number of unmyelinated axons for all subjects.

ψ_M was determined by changes in JC-1 fluorescence. JC-1 exists either as a green fluorescent monomer at depolarized membrane potentials or as an orange-red fluorescent aggregate at hyperpolarized membrane potentials. Decrease in ψ_M leads to a decrease in fluorescent red-orange signal with a concomitant increase in green fluorescence, leading to lower values for the orange-red/green fluorescence ratio. ψ_M was determined as a ratio of orange-red fluorescence to green fluorescent signal. The red and green fluorescence signals in the axon shaft ROIs were determined for individual neurons using ImageJ. Regions next to the ROIs were measured to calculate the background fluorescence intensity for each channel, and the average background fluorescence intensity was subtracted from average fluorescence intensities of ROIs. For measuring JC-1 fluorescence in DRGs transfected with expression construct, following JC-1 live cell imaging, cells were fixed and stained with Myc and NF. The axon shaft ROIs used for measuring JC-1 fluorescence were determined by overlaying the JC-1 images with the Myc and NF images. Mitochondrial membrane potential for each ROI was calculated by dividing orange-red fluorescent signal by the green fluorescent signal. A minimum of 25 ROIs was used to calculate the mitochondrial membrane potential for each treatment group.

Statistical analysis

Prism (GraphPad) or Kaleidagraph (Synergy) software was used for all analysis. Data distributions were assumed to be normal. Statistical tests used were (as indicated in each figure legends) one-way ANOVA with Bonferonni's post hoc correction (Fig. 1, A and C; Fig. 2, A and C; Fig. 3, C and D; Fig. S2, B–D; and Fig. S4, F–H); two-way ANOVA with Tukey's post hoc correction (Fig. 4, A–F and H; Fig. 5; Fig. 6 A; Fig. 7, A, C, D, H, and I; Fig. S1 C; and Fig. S5 A); ANOVA with Holm–Sidak's multiple comparisons (Fig. 2, D–F; and Fig. S3, C–G); two-tailed Student's t test (Fig. 6

B); and Student's *t* test using matched-pairs signed-rank test (Fig. S4, A and B). For comparison of matched pairs across different experiments, one-way ANOVA with pairwise comparison and Tukey's post hoc tests was used (Fig. 6, G–I; Fig. 7, B, F, and G; and Fig. S7, B–D). Kolmogorov–Smirnov *t* test was used for comparing across pooled time point groups (Fig. S5 C). P values <0.05 were considered significant.

Online supplemental material

In Fig. S1, TubA increases Ac-α-tubulin levels without affecting histone acetylation (companion data for Fig. 1). In Fig. S2, inhibition of HDAC6 triggers rapid increase in axonal acetylated α-tubulin (companion data for Fig. 1). In Fig. S3, HDAC6 inhibition causes a net shift in mitochondrial transport toward anterograde movement (companion data for Fig. 2). In Fig. S4, growth cones of HDAC6-depleted DRG neurons are protected from collapse after mitochondrial ablation (companion data for Fig. 3). In Fig. S5, MAG attenuates mitochondrial transport through axon-intrinsic mechanisms (companion data for Fig. 5). Fig. S6 shows acetylation of Miro1 in DRG neurons (companion data for Fig. 6). In Fig. S7, Myc-Miro1 mutants localize to axonal mitochondria (companion data for Fig. 7).

Acknowledgments

Author contributions: conceptualization – A.L. Kalinski, A.N. Kar, G. Schiavo, R.J. Giger, B. Langley, and J.L. Twiss; data curation – A.L. Kalinski, A.N. Kar, A.P. Tosolini, and J.N. Sleigh; formal analysis – A.L. Kalinski, A.N. Kar, A.P. Tosolini, J.N. Sleigh, and A. Hawthorne; funding acquisition – L.A. Havton, G. Schiavo, R.J. Giger, B. Langley, and J.L. Twiss; investigation – A.L. Kalinski, A.N. Kar, J. Craver, A.P. Tosolini, J.N. Sleigh, S.J. Lee, A. Hawthorne, P. Brito-Vargas, S. Miller-Randolph, R. Passino, L. Shi, V.S.C. Wong, C. Picci, D.S. Smith, D.E. Willis, and L.A. Havton; methodology – A.L. Kalinski, A.N. Kar, A.P. Tosolini, J.N. Sleigh, S.J. Lee, A. Hawthorne, D.S. Smith, L.A. Havton, G. Schiavo, R.J. Giger, and J.L. Twiss; project administration – S. Miller-Randolph, G. Schiavo, R.J. Giger, B. Langley, and J.L. Twiss; resources – S.J. Lee; supervision – D.S. Smith, D.E. Willis, L.A. Havton, G. Schiavo, R.J. Giger, B. Langley, and J.L. Twiss; validation – A.L. Kalinski and A.N. Kar; writing – original draft – A.L. Kalinski, A.N. Kar, A.P. Tosolini, J.N. Sleigh, and J.L. Twiss; writing – review and editing – A.L. Kalinski, A.N. Kar, A.P. Tosolini, J.N. Sleigh, D.S. Smith, D.E. Willis, L.A. Havton, G. Schiavo, R.J. Giger, B. Langley, and J.L. Twiss.

References

Andrews, S., J. Gilley, and M.P. Coleman. 2010. Difference Tracker: ImageJ plugins for fully automated analysis of multiple axonal transport parameters. *J. Neurosci. Methods.* 193:281–287. https://doi.org/10.1016/j.jneumeth.2010.09.007

Baas, P.W., and M.M. Black. 1990. Individual microtubules in the axon consist of domains that differ in both composition and stability. *J. Cell Biol.* 111:495–509. https://doi.org/10.1083/jcb.111.2.495

Babic, M., G.J. Russo, A.J. Wellington, R.M. Sangston, M. Gonzalez, and K.E. Zinsmaier. 2015. Miro's N-terminal GTPase domain is required for transport of mitochondria into axons and dendrites. *J. Neurosci.* 35:5754–5771. https://doi.org/10.1523/JNEUROSCI.1035-14.2015

Benowitz, L.I., Z. He, and J.L. Goldberg. 2017. Reaching the brain: Advances in optic nerve regeneration. *Exp. Neurol.* 287:365–373. https://doi.org/10.1016/j.expneurol.2015.12.015

Benoy, V., L. Van Helleputte, R. Prior, C. d'Ydewalle, W. Haeck, N. Geens, W. Scheveneels, B. Schevenels, M.Z. Cader, K. Talbot, et al. 2018. HDAC6 is a therapeutic target in mutant GARS-induced Charcot-Marie-Tooth disease. *Brain.* 141:673–687. https://doi.org/10.1093/brain/awx375

Birsa, N., R. Norkett, T. Wauer, T.E. Mevissen, H.C. Wu, T. Foltynie, K. Bhatia, W.D. Hirst, D. Komander, H. Plun-Favreau, and J.T. Kittler. 2014. Lysine 27 ubiquitination of the mitochondrial transport protein Miro is dependent on serine 65 of the Parkin ubiquitin ligase. *J. Biol. Chem.* 289:14569–14582. https://doi.org/10.1074/jbc.M114.563031

Butler, K.V., J. Kalin, C. Brochier, G. Vistoli, B. Langley, and A.P. Kozikowski. 2010. Rational design and simple chemistry yield a superior, neuroprotective HDAC6 inhibitor, tubastatin A. *J. Am. Chem. Soc.* 132:10842–10846. https://doi.org/10.1021/ja102758v

Cai, D., J. Qiu, Z. Cao, M. McAtee, B.S. Bregman, and M.T. Filbin. 2001. Neuronal cyclic AMP controls the developmental loss in ability of axons to regenerate. *J. Neurosci.* 21:4731–4739. https://doi.org/10.1523/JNEUROSCI.21-13-04731.2001

Cambray-Deakin, M.A., and R.D. Burgoyne. 1987. Posttranslational modifications of alpha-tubulin: acetylated and detyrosinated forms in axons of rat cerebellum. *J. Cell Biol.* 104:1569–1574. https://doi.org/10.1083/jcb.104.6.1569

Cartoni, R., M.W. Norsworthy, F. Bei, C. Wang, S. Li, Y. Zhang, C.V. Gabel, T.L. Schwarz, and Z. He. 2016. The Mammalian-Specific Protein Armcx1 Regulates Mitochondrial Transport during Axon Regeneration. *Neuron.* 92:1294–1307. https://doi.org/10.1016/j.neuron.2016.10.060

Cartoni, R., G. Pekkurnaz, C. Wang, T.L. Schwarz, and Z. He. 2017. A high mitochondrial transport rate characterizes CNS neurons with high axonal regeneration capacity. *PLoS One.* 12:e0184672. https://doi.org/10.1371/journal.pone.0184672

Chang, K.T., R.F. Niescier, and K.T. Min. 2011. Mitochondrial matrix Ca2+ as an intrinsic signal regulating mitochondrial motility in axons. *Proc. Natl. Acad. Sci. USA.* 108:15456–15461. https://doi.org/10.1073/pnas.1106862108

Chen, S., G.C. Owens, H. Makarenkova, and D.B. Edelman. 2010. HDAC6 regulates mitochondrial transport in hippocampal neurons. *PLoS One.* 5:e10848. https://doi.org/10.1371/journal.pone.0010848

Choudhary, C., C. Kumar, F. Gnad, M.L. Nielsen, M. Rehman, T.C. Walther, J.V. Olsen, and M. Mann. 2009. Lysine acetylation targets protein complexes and co-regulates major cellular functions. *Science.* 325:834–840. https://doi.org/10.1126/science.1175371

d'Ydewalle, C., J. Krishnan, D.M. Chiheb, P. Van Damme, J. Irobi, A.P. Kozikowski, P. Vanden Berghe, V. Timmerman, W. Robberecht, and L. Van Den Bosch. 2011. HDAC6 inhibitors reverse axonal loss in a mouse model of mutant HSPB1-induced Charcot-Marie-Tooth disease. *Nat. Med.* 17:968–974. https://doi.org/10.1038/nm.2396

Dompierre, J.P., J.D. Godin, B.C. Charrin, F.P. Cordelières, S.J. King, S. Humbert, and F. Saudou. 2007. Histone deacetylase 6 inhibition compensates for the transport deficit in Huntington's disease by increasing tubulin acetylation. *J. Neurosci.* 27:3571–3583. https://doi.org/10.1523/JNEUROSCI.0037-07.2007

Duffy, P., A. Schmandke, A. Schmandke, J. Sigworth, S. Narumiya, W.B. Cafferty, and S.M. Strittmatter. 2009. Rho-associated kinase II (ROCKII) limits axonal growth after trauma within the adult mouse spinal cord. *J. Neurosci.* 29:15266–15276. https://doi.org/10.1523/JNEUROSCI.4650-09.2009

Ertürk, A., F. Hellal, J. Enes, and F. Bradke. 2007. Disorganized microtubules underlie the formation of retraction bulbs and the failure of axonal regeneration. *J. Neurosci.* 27:9169–9180. https://doi.org/10.1523/JNEUROSCI.0612-07.2007

Flatau, G., E. Lemichez, M. Gauthier, P. Chardin, S. Paris, C. Fiorentini, and P. Boquet. 1997. Toxin-induced activation of the G protein p21 Rho by deamidation of glutamine. *Nature.* 387:729–733. https://doi.org/10.1038/42743

Fournier, A.E., B.T. Takizawa, and S.M. Strittmatter. 2003. Rho kinase inhibition enhances axonal regeneration in the injured CNS. *J. Neurosci.* 23:1416–1423. https://doi.org/10.1523/JNEUROSCI.23-04-01416.2003

Fransson, S., A. Ruusala, and P. Aspenström. 2006. The atypical Rho GTPases Miro-1 and Miro-2 have essential roles in mitochondrial trafficking. *Biochem. Biophys. Res. Commun.* 344:500–510. https://doi.org/10.1016/j.bbrc.2006.03.163

Fujita, Y., and T. Yamashita. 2014. Axon growth inhibition by RhoA/ROCK in the central nervous system. *Front. Neurosci.* 8:338. https://doi.org/10.3389/fnins.2014.00338

Gibbs, K.L., B. Kalmar, J.N. Sleigh, L. Greensmith, and G. Schiavo. 2016. In vivo imaging of axonal transport in murine motor and sensory neurons. *J. Neurosci. Methods.* 257:26–33. https://doi.org/10.1016/j.jneumeth.2015.09.018

Graf, S.A., S.E. Haigh, E.D. Corson, and O.S. Shirihai. 2004. Targeting, import, and dimerization of a mammalian mitochondrial ATP binding cassette (ABC) transporter, ABCB10 (ABC-me). *J. Biol. Chem.* 279:42954–42963. https://doi.org/10.1074/jbc.M405040200

Guo, W., M. Naujock, L. Fumagalli, T. Vandoorne, P. Baatsen, R. Boon, L. Ordovás, A. Patel, M. Welters, T. Vanwelden, et al. 2017. HDAC6 inhibition reverses axonal transport defects in motor neurons derived from FUS-ALS patients. *Nat. Commun.* 8:861. https://doi.org/10.1038/s41467-017-00911-y

Hammond, J.W., K. Griffin, G.T. Jih, J. Stuckey, and K.J. Verhey. 2008. Cooperative versus independent transport of different cargoes by Kinesin-1. *Traffic.* 9:725–741. https://doi.org/10.1111/j.1600-0854.2008.00722.x

Hellal, F., A. Hurtado, J. Ruschel, K.C. Flynn, C.J. Laskowski, M. Umlauf, L.C. Kapitein, D. Strikis, V. Lemmon, J. Bixby, et al. 2011. Microtubule stabilization reduces scarring and causes axon regeneration after spinal cord injury. *Science.* 331:928–931. https://doi.org/10.1126/science.1201148

Henley, J.R., K.H. Huang, D. Wang, and M.M. Poo. 2004. Calcium mediates bidirectional growth cone turning induced by myelin-associated glycoprotein. *Neuron.* 44:909–916. https://doi.org/10.1016/j.neuron.2004.11.030

Hubbert, C., A. Guardiola, R. Shao, Y. Kawaguchi, A. Ito, A. Nixon, M. Yoshida, X.F. Wang, and T.P. Yao. 2002. HDAC6 is a microtubule-associated deacetylase. *Nature.* 417:455–458. https://doi.org/10.1038/417455a

Joshi, A.R., I. Bobylev, G. Zhang, K.A. Sheikh, and H.C. Lehmann. 2015. Inhibition of Rho-kinase differentially affects axon regeneration of peripheral motor and sensory nerves. *Exp. Neurol.* 263:28–38. https://doi.org/10.1016/j.expneurol.2014.09.012

Kazlauskaite, A., V. Kelly, C. Johnson, C. Baillie, C.J. Hastie, M. Peggie, T. Macartney, H.I. Woodroof, D.R. Alessi, P.G. Pedrioli, and M.M. Muqit. 2014. Phosphorylation of Parkin at Serine65 is essential for activation: elaboration of a Miro1 substrate-based assay of Parkin E3 ligase activity. *Open Biol.* 4:130213. https://doi.org/10.1098/rsob.130213

Kim, C., H. Choi, E.S. Jung, W. Lee, S. Oh, N.L. Jeon, and I. Mook-Jung. 2012. HDAC6 inhibitor blocks amyloid beta-induced impairment of mitochondrial transport in hippocampal neurons. *PLoS One.* 7:e42983. https://doi.org/10.1371/journal.pone.0042983

Krukowski, K., J. Ma, O. Golonzhka, G.O. Laumet, T. Gutti, J.H. van Duzer, R. Mazitschek, M.B. Jarpe, C.J. Heijnen, and A. Kavelaars. 2017. HDAC6 inhibition effectively reverses chemotherapy-induced peripheralneuropathy. *Pain.* 158:1126–1137. https://doi.org/10.1097/j.pain.0000000000000893

Lahm, A., C. Paolini, M. Pallaoro, M.C. Nardi, P. Jones, P. Neddermann, S. Sambucini, M.J. Bottomley, P. Lo Surdo, A. Carfí, et al. 2007. Unraveling the hidden catalytic activity of vertebrate class IIa histone deacetylases. *Proc. Natl. Acad. Sci. USA.* 104:17335–17340. https://doi.org/10.1073/pnas.0706487104

Lee, K.S., and B. Lu. 2014. The myriad roles of Miro in the nervous system: axonal transport of mitochondria and beyond. *Front. Cell. Neurosci.* 8:330. https://doi.org/10.3389/fncel.2014.00330

Lee, S.J., Z. Li, A. Litan, S. Yoo, and S.A. Langhans. 2015. EGF-induced sodium influx regulates EGFR trafficking through HDAC6 and tubulin acetylation. *BMC Cell Biol.* 16:24. https://doi.org/10.1186/s12860-015-0070-8

Lee, Z.W., S.M. Kweon, B.C. Kim, S.H. Leem, I. Shin, J.H. Kim, and K.S. Ha. 1998. Phosphatidic acid-induced elevation of intracellular Ca2+ is mediated by RhoA and H2O2 in Rat-2 fibroblasts. *J. Biol. Chem.* 273:12710–12715. https://doi.org/10.1074/jbc.273.21.12710

Lewis, T.L. Jr., G.F. Turi, S.K. Kwon, A. Losonczy, and F. Polleux. 2016. Progressive Decrease of Mitochondrial Motility during Maturation of Cortical Axons In Vitro and In Vivo. *Curr. Biol.* 26:2602–2608. https://doi.org/10.1016/j.cub.2016.07.064

Li, M., J. Luo, C.L. Brooks, and W. Gu. 2002. Acetylation of p53 inhibits its ubiquitination by Mdm2. *J. Biol. Chem.* 277:50607–50611. https://doi.org/10.1074/jbc.C200578200

Liao, P.C., L.C. Tandarich, and P.J. Hollenbeck. 2017. ROS regulation of axonal mitochondrial transport is mediated by Ca2+ and JNK in Drosophila. *PLoS One.* 12:e0178105. https://doi.org/10.1371/journal.pone.0178105

Lin, M.Y., and Z.H. Sheng. 2015. Regulation of mitochondrial transport in neurons. *Exp. Cell Res.* 334:35–44. https://doi.org/10.1016/j.yexcr.2015.01.004

Lin, S., K. Nazif, A. Smith, P.W. Baas, and G.M. Smith. 2015. Histone acetylation inhibitors promote axon growth in adult dorsal root ganglia neurons. *J. Neurosci. Res.* 93:1215–1228. https://doi.org/10.1002/jnr.23573

Lundby, A., K. Lage, B.T. Weinert, D.B. Bekker-Jensen, A. Secher, T. Skovgaard, C.D. Kelstrup, A. Dmytriyev, C. Choudhary, C. Lundby, and J.V. Olsen. 2012. Proteomic analysis of lysine acetylation sites in rat tissues reveals organ specificity and subcellular patterns. *Cell Reports.* 2:419–431. https://doi.org/10.1016/j.celrep.2012.07.006

Matsuyama, A., T. Shimazu, Y. Sumida, A. Saito, Y. Yoshimatsu, D. Seigneurin-Berny, H. Osada, Y. Komatsu, N. Nishino, S. Khochbin, et al. 2002. In vivo destabilization of dynamic microtubules by HDAC6-mediated deacetylation. *EMBO J.* 21:6820–6831. https://doi.org/10.1093/emboj/cdf682

Merianda, T.T., A.C. Lin, J.S. Lam, D. Vuppalanchi, D.E. Willis, N. Karin, C.E. Holt, and J.L. Twiss. 2009. A functional equivalent of endoplasmic reticulum and Golgi in axons for secretion of locally synthesized proteins. *Mol. Cell. Neurosci.* 40:128–142. https://doi.org/10.1016/j.mcn.2008.09.008

Miller, K.E., and M.P. Sheetz. 2004. Axonal mitochondrial transport and potential are correlated. *J. Cell Sci.* 117:2791–2804. https://doi.org/10.1242/jcs.01130

Mo, Z., X. Zhao, H. Liu, Q. Hu, X.Q. Chen, J. Pham, N. Wei, Z. Liu, J. Zhou, R.W. Burgess, et al. 2018. Aberrant GlyRS-HDAC6 interaction linked to axonal transport deficits in Charcot-Marie-Tooth neuropathy. *Nat. Commun.* 9:1007. https://doi.org/10.1038/s41467-018-03461-z

Mohan, R., A.P. Tosolini, and R. Morris. 2015. Intramuscular Injections Along the Motor End Plates: A Minimally Invasive Approach to Shuttle Tracers Directly into Motor Neurons. *J. Vis. Exp.* 101:e52846.

Niescier, R.F., K. Hong, D. Park, and K.T. Min. 2018. MCU Interacts with Miro1 to Modulate Mitochondrial Functions in Neurons. *J. Neurosci.* 38:4666–4677. https://doi.org/10.1523/JNEUROSCI.0504-18.2018

Paillusson, S., R. Stoica, P. Gomez-Suaga, D.H.W. Lau, S. Mueller, T. Miller, and C.C.J. Miller. 2016. There's Something Wrong with my MAM; the ER-Mitochondria Axis and Neurodegenerative Diseases. *Trends Neurosci.* 39:146–157. https://doi.org/10.1016/j.tins.2016.01.008

Pareyson, D., P. Saveri, A. Sagnelli, and G. Piscosquito. 2015. Mitochondrial dynamics and inherited peripheral nerve diseases. *Neurosci. Lett.* 596:66–77. https://doi.org/10.1016/j.neulet.2015.04.001

Rishal, I., O. Golani, M. Rajman, B. Costa, K. Ben-Yaakov, Z. Schoenmann, A. Yaron, R. Basri, M. Fainzilber, and M. Galun. 2013. WIS-NeuroMath

enables versatile high throughput analyses of neuronal processes. *Dev. Neurobiol.* 73:247–256. https://doi.org/10.1002/dneu.22061

Rivieccio, M.A., C. Brochier, D.E. Willis, B.A. Walker, M.A. D'Annibale, K. McLaughlin, A. Siddiq, A.P. Kozikowski, S.R. Jaffrey, J.L. Twiss, et al. 2009. HDAC6 is a target for protection and regeneration following injury in the nervous system. *Proc. Natl. Acad. Sci. USA.* 106:19599–19604. https://doi.org/10.1073/pnas.0907935106

Rui, Y., and J.Q. Zheng. 2016. Amyloid β oligomers elicit mitochondrial transport defects and fragmentation in a time-dependent and pathway-specific manner. *Mol. Brain.* 9:79. https://doi.org/10.1186/s13041-016-0261-z

Ruschel, J., F. Hellal, K.C. Flynn, S. Dupraz, D.A. Elliott, A. Tedeschi, M. Bates, C. Sliwinski, G. Brook, K. Dobrindt, et al. 2015. Axonal regeneration. Systemic administration of epothilone B promotes axon regeneration after spinal cord injury. *Science.* 348:347–352. https://doi.org/10.1126/science.aaa2958

Sainath, R., L. Armijo-Weingart, A. Ketscheck, Z. Xu, S. Li, and G. Gallo. 2017. Chondroitin sulfate proteoglycans negatively regulate the positioning of mitochondria and endoplasmic reticulum to distal axons. *Dev. Neurobiol.* 77:1351–1370. https://doi.org/10.1002/dneu.22535

Sano, Y., W. Watanabe, and S. Matsunaga. 2014. Chromophore-assisted laser inactivation--towards a spatiotemporal-functional analysis of proteins, and the ablation of chromatin, organelle and cell function. *J. Cell Sci.* 127:1621–1629. https://doi.org/10.1242/jcs.144527

Saxton, W.M., and P.J. Hollenbeck. 2012. The axonal transport of mitochondria. *J. Cell Sci.* 125:2095–2104. https://doi.org/10.1242/jcs.053850

Schmidt, G., P. Sehr, M. Wilm, J. Selzer, M. Mann, and K. Aktories. 1997. Gln 63 of Rho is deamidated by Escherichia coli cytotoxic necrotizing factor-1. *Nature.* 387:725–729. https://doi.org/10.1038/42735

Schweigreiter, R., A.R. Walmsley, B. Niederöst, D.R. Zimmermann, T. Oertle, E. Casademunt, S. Frentzel, G. Dechant, A. Mir, and C.E. Bandtlow. 2004. Versican V2 and the central inhibitory domain of Nogo-A inhibit neurite growth via p75NTR/NgR-independent pathways that converge at RhoA. *Mol. Cell. Neurosci.* 27:163–174. https://doi.org/10.1016/j.mcn.2004.06.004

Shibuya, T., and Y. Tsujimoto. 2012. Deleterious effects of mitochondrial ROS generated by KillerRed photodynamic action in human cell lines and C. elegans. *J. Photochem. Photobiol. B.* 117:1–12. https://doi.org/10.1016/j.jphotobiol.2012.08.005

Shlevkov, E., T. Kramer, J. Schapansky, M.J. LaVoie, and T.L. Schwarz. 2016. Miro phosphorylation sites regulate Parkin recruitment and mitochondrial motility. *Proc. Natl. Acad. Sci. USA.* 113:E6097–E6106. https://doi.org/10.1073/pnas.1612283113

Sleigh, J., and G. Schiavo. 2016. *Older but not slower: aging does not alter axonal transport dynamics of signalling endosomes in vivo.* Matters. https://doi.org/10.19185/matters.201605000018.

Smith, G.M., and G. Gallo. 2018. The role of mitochondria in axon development and regeneration. *Dev. Neurobiol.* 78:221–237. https://doi.org/10.1002/dneu.22546

Snow, D.M., P.B. Atkinson, T.D. Hassinger, P.C. Letourneau, and S.B. Kater. 1994. Chondroitin sulfate proteoglycan elevates cytoplasmic calcium in DRG neurons. *Dev. Biol.* 166:87–100. https://doi.org/10.1006/dbio.1994.1298

Spillane, M., A. Ketschek, T.T. Merianda, J.L. Twiss, and G. Gallo. 2013. Mitochondria coordinate sites of axon branching through localized intra-axonal protein synthesis. *Cell Reports.* 5:1564–1575. https://doi.org/10.1016/j.celrep.2013.11.022

Steketee, M.B., S.N. Moysidis, J.E. Weinstein, A. Kreymerman, J.P. Silva, S. Iqbal, and J.L. Goldberg. 2012. Mitochondrial dynamics regulate growth cone motility, guidance, and neurite growth rate in perinatal retinal ganglion cells in vitro. *Invest. Ophthalmol. Vis. Sci.* 53:7402–7411. https://doi.org/10.1167/iovs.12-10298

Tom, V.J., M.P. Steinmetz, J.H. Miller, C.M. Doller, and J. Silver. 2004. Studies on the development and behavior of the dystrophic growth cone, the hallmark of regeneration failure, in an in vitro model of the glial scar and after spinal cord injury. *J. Neurosci.* 24:6531–6539. https://doi.org/10.1523/JNEUROSCI.0994-04.2004

Twiss, J.L., D.S. Smith, B. Chang, and E.M. Shooter. 2000. Translational control of ribosomal protein L4 mRNA is required for rapid neurite regeneration. *Neurobiol. Dis.* 7:416–428. https://doi.org/10.1006/nbdi.2000.0293

Van Helleputte, L., M. Kater, D.P. Cook, C. Eykens, E. Rossaert, W. Haeck, T. Jaspers, N. Geens, P. Vanden Berghe, C. Gysemans, et al. 2018. Inhibition of histone deacetylase 6 (HDAC6) protects against vincristine-induced peripheral neuropathies and inhibits tumor growth. *Neurobiol. Dis.* 111:59–69. https://doi.org/10.1016/j.nbd.2017.11.011

van Spronsen, M., M. Mikhaylova, J. Lipka, M.A. Schlager, D.J. van den Heuvel, M. Kuijpers, P.S. Wulf, N. Keijzer, J. Demmers, L.C. Kapitein, et al. 2013. TRAK/Milton motor-adaptor proteins steer mitochondrial trafficking to axons and dendrites. *Neuron.* 77:485–502. https://doi.org/10.1016/j.neuron.2012.11.027

Verdel, A., S. Curtet, M.P. Brocard, S. Rousseaux, C. Lemercier, M. Yoshida, and S. Khochbin. 2000. Active maintenance of mHDA2/mHDAC6 histone-deacetylase in the cytoplasm. *Curr. Biol.* 10:747–749. https://doi.org/10.1016/S0960-9822(00)00542-X

Wagner, S.A., P. Beli, B.T. Weinert, C. Schölz, C.D. Kelstrup, C. Young, M.L. Nielsen, J.V. Olsen, C. Brakebusch, and C. Choudhary. 2012. Proteomic analyses reveal divergent ubiquitylation site patterns in murine tissues. *Mol. Cell. Proteomics.* 11:1578–1585. https://doi.org/10.1074/mcp.M112.017905

Willis, D.E., E.A. van Niekerk, Y. Sasaki, M. Mesngon, T.T. Merianda, G.G. Williams, M. Kendall, D.S. Smith, G.J. Bassell, and J.L. Twiss. 2007. Extracellular stimuli specifically regulate localized levels of individual neuronal mRNAs. *J. Cell Biol.* 178:965–980. https://doi.org/10.1083/jcb.200703209

Wong, V.S.C., C. Picci, M. Swift, M. Levinson, D. Willis, and B. Langley. 2018. Alpha-Tubulin acetyltransferase is a novel target mediating growth inhibitory effects of chondroitin sulfate proteoglycans and myelin-associated glycoprotein. *eNeuro.*. https://doi.org/10.1523/ENEURO.0240-17.2018

Zhang, Y., N. Li, C. Caron, G. Matthias, D. Hess, S. Khochbin, and P. Matthias. 2003. HDAC-6 interacts with and deacetylates tubulin and microtubules in vivo. *EMBO J.* 22:1168–1179. https://doi.org/10.1093/emboj/cdg115

Zhang, Y., S. Kwon, T. Yamaguchi, F. Cubizolles, S. Rousseaux, M. Kneissel, C. Cao, N. Li, H.L. Cheng, K. Chua, et al. 2008. Mice lacking histone deacetylase 6 have hyperacetylated tubulin but are viable and develop normally. *Mol. Cell. Biol.* 28:1688–1701. https://doi.org/10.1128/MCB.01154-06

Zhou, B., P. Yu, M.Y. Lin, T. Sun, Y. Chen, and Z.H. Sheng. 2016. Facilitation of axon regeneration by enhancing mitochondrial transport and rescuing energy deficits. *J. Cell Biol.* 214:103–119. https://doi.org/10.1083/jcb.201605101